Beyond the chemical master equation: stochastic chemical kinetics coupled with auxiliary processes

Davin Lunz, Gregory Batt, Jakob Ruess, Joseph Frédéric Bonnans

▶ **To cite this version:**

Davin Lunz, Gregory Batt, Jakob Ruess, Joseph Frédéric Bonnans. Beyond the chemical master equation: stochastic chemical kinetics coupled with auxiliary processes. 2020. hal-02991103v1

HAL Id: hal-02991103

https://inria.hal.science/hal-02991103v1

Preprint submitted on 5 Nov 2020 (v1), last revised 14 Sep 2021 (v2)

HAL is a multi-disciplinary open access archive for the deposit and dissemination of scientific research documents, whether they are published or not. The documents may come from teaching and research institutions in France or abroad, or from public or private research centers.

L'archive ouverte pluridisciplinaire **HAL**, est destinée au dépôt et à la diffusion de documents scientifiques de niveau recherche, publiés ou non, émanant des établissements d'enseignement et de recherche français ou étrangers, des laboratoires publics ou privés.

Beyond the chemical master equation: stochastic chemical kinetics coupled with auxiliary processes

Davin Lunz[1,2,3,4], Gregory Batt[3,4], Jakob Ruess[3,4], and J. Frédéric Bonnans[1,2]

[1] *Inria Saclay – Île de France, 91120 Palaiseau, France*
[2] *École Polytechnique, CMAP 91128 Palaiseau, France*
[3] *Inria Paris, 75589 Paris, France*
[4] *Institut Pasteur, 75015 Paris, France*

Abstract

The chemical master equation and its continuum approximations are indispensable tools in the modeling of chemical reaction networks. These are routinely used to capture complex nonlinear phenomena such as multimodality as well as transient events such as first-passage times, that accurately characterise a plethora of biological and chemical processes. However, some mechanisms, such as heterogeneous cellular growth or phenotypic selection at the population level, cannot be represented by the master equation and thus have been tackled separately. In this work, we propose a unifying framework that augments the chemical master equation to capture such auxiliary dynamics, and we develop and analyse a numerical solver that accurately simulates the system dynamics. We showcase these contributions by casting a diverse array of examples from the literature within this framework, and apply the solver to both match and extend previous studies. Analytical calculations performed for each example validate our numerical results and benchmark the solver implementation.

1 Introduction

The chemical master equation (CME) [1] governs the evolution of the probability distribution of the configuration, or state, of a reaction network. Typically, the configuration describes the number of molecules of various species, such as chemical reactants undergoing reactions. The CME and its continuum approximations, in particular the Fokker–Planck approximation [2], are fundamental modeling tools used for describing chemical reaction networks. These reaction networks find broad application across the quantitative sciences, providing accurate descriptions of a wide variety of chemical, biological and social phenomena [3]. Crucially, this family of models accounts for stochasticity inherent in reaction processes that play functional roles in biochemical contexts [4, 5]. In a population of individuals each governed by identical reaction kinetics, such as gene expression in a population of cells, this stochasticity manifests in cell-to-cell variability. When a state-dependent selection pressure is exerted upon the population, for example, phenotypic growth or cell-fate decisions, individuals are affected heterogeneously due to this cell-to-cell variability [6]. The dynamics of such phenomena cannot be captured simply by a stochastic reaction network [7]. Models that incorporate population-level selection may break detailed balance and introduce nonlinearity into the master equation [8], rendering explicit solutions unknown in all but the simplest of circumstances [9]. We depict the example of state-dependent growth in a population of cells in Fig. 1.

Recently, this problem was addressed in [10] by embedding the internal single-cell state into a global state counter, which sums the number of cells in each possible configuration. The biochemistry governing the state of each cell is encapsulated by alterations to the global state counter. In this way, the single-cell kinetics may be coupled to population-level dynamics. While conceptually appealing, this formalism is immensely cumbersome. Furthermore, it embeds the CME into a population-level description that inherits, and even inflates, the formidable computational difficulty. To address this, a moment-closure framework is derived that ultimately requires ad-hoc assumptions to close the moment hierarchy.

In this study, we develop a framework that reaches beyond the classical master equation to incorporate such population-level processes without the need for burdensome construction. Our starting point is the classical CME. Keeping in mind that when the typical number of a species is large the CME is challenging to solve, we allow a continuum approximation in the form of the Fokker–Planck equation.

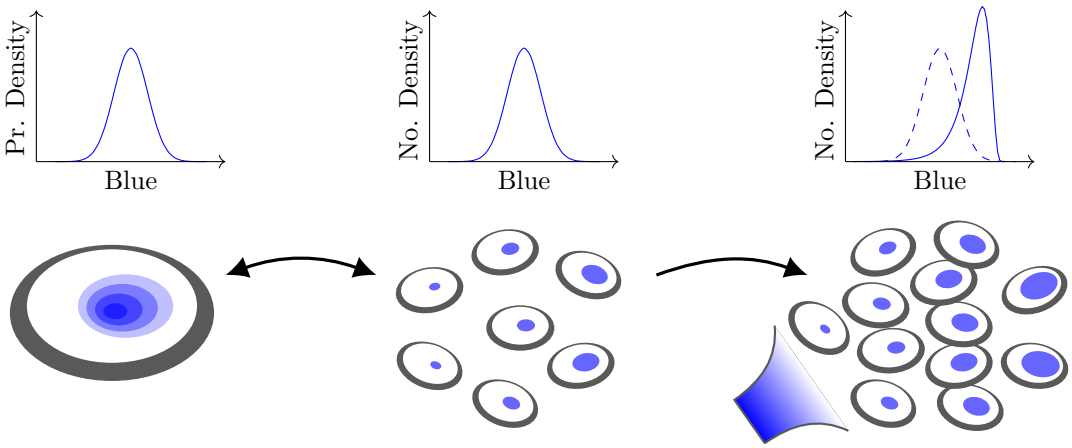

Figure 1: Schematic depiction of the concentration of a nominal "blue" chemical species within a cell that is the downstream result of some chemical reaction network. The probability density of concentration in a single cell (left) is identical to the number density in a large population of identical cells (centre). However, when a state-dependent pressure (such as amplified growth for higher blue concentration) is exerted on the population (right), the distribution is affected in a way that may not be encapsulated by a classical CME. This paper studies a framework in which chemical reaction networks coupled to such auxiliary processes are captured, and introduces a software package to simulate their dynamics.

We also allow non-local transitions to incorporate phenomena discontinuous in state such as cell division and fragmentation [11, ch. 4], as well as burst-like phenomena where production machinery operates on timescales significantly shorter than the timescale of interest [12], such as in bursty protein production. This class of models finds application beyond biochemical physics, such as in communications protocols [13].

Crucially, not all species need be cast in the continuum, and thus we retain a hybrid structure: species of typically large number are in the continuum, while the remaining species retain a discrete description. This discrete structure allows us not only to capture discrete molecule numbers, but also to model abstract system states. For example, we may consider transcription factors in gene expression in a bound or unbound state, or distinguish cells based on phases of the cell cycle, as well as cell-fate decisions such as differentiation and recombination. This demonstrates the importance of retaining a discrete structure in the framework, which allows us to capture both discrete molecule numbers, as well as discrete abstract states that correspond to physical system configurations. In this study, we leverage the discrete structure to capture first-passage times, providing insights that lend a new and extended perspective to existing results.

Some population-level processes may be resolved by leveraging this same discrete structure in non-physical ways. In this case, the discrete states are not simply abstract states, as they may no longer correspond to physical configurations at all. For example, we may need to consider negative "reaction" rates, breaching the physical description of a classical chemical reaction network. We highlight the distinction by calling these phantom states. By constructing systems incorporating phantom states, we show that we are able to couple CME dynamics to non-standard processes by casting them within our general framework.

Finally, we show how other classes of auxiliary processes fall within this framework, such as growth–fragmentation processes used to describe cell growth and mitosis (that is, cell division), as well as several other physical phenomena.

With the goal of open and collaborative progress, we make our code publicly available [14] in the hope that this modeling tool can be of broader use for the community. The code is generic and has been written for arbitrary reaction networks, growth–fragmentation and similar models. The interface is intended to be straightforward for the first-time user, while also allowing more advanced control of the numerical scheme, including discretisation and time-stepping details.

The rest of the paper is structured as follows. In Section 2.1 we introduce the encompassing framework by defining the class of problems under consideration. In Section 2.2 we outline the numerical software developed to solve problems cast in this framework. In Section 3 we present case studies of auxiliary processes not classically captured by the CME: a first-passage time problem in self-regulated gene expression (Section 3.1), a birth–death process under population-wide growth pressure (Section 3.2),

and a growth–fragmentation model (Section 3.3). Finally, we discuss the results and their implications in Section 4. For the sake of completeness, in Appendix A we include an extensive description of the numerical scheme implemented in the software.

2 Methodology

2.1 Augmented CME framework

We consider a stochastic reaction network of d species written in vector form $\boldsymbol{X} := (X_1, X_2, \ldots, X_d)^T$, undergoing reactions labeled by $i \in \mathcal{I}$, which we write as

$$\boldsymbol{c}_i \cdot \boldsymbol{X} \xrightarrow{R_i(\boldsymbol{X},t)} \boldsymbol{d}_i \cdot \boldsymbol{X}, \tag{1}$$

for reactant species and quantities determined by $\boldsymbol{c}_i \in \mathbb{Z}^d$ and product species and quantities determined by $\boldsymbol{d}_i \in \mathbb{Z}^d$. The reaction rate is described by R_i and may depend on the system state $\boldsymbol{X}$ and time t. The corresponding chemical master equation (CME) takes the form

$$\frac{\partial P(\boldsymbol{X},t)}{\partial t} = \sum_{i\in\mathcal{I}} R_i(\boldsymbol{X}+\boldsymbol{c}_i-\boldsymbol{d}_i,t)P(\boldsymbol{X}+\boldsymbol{c}_i-\boldsymbol{d}_i,t) - R_i(\boldsymbol{X},t)P(\boldsymbol{X},t). \tag{2}$$

We assume that the species typically occur in large numbers, and seek to approximate the discrete description on the continuum. Defining $\boldsymbol{e}_i := \boldsymbol{d}_i - \boldsymbol{c}_i$, the Fokker–Planck approximation [15, Ch. 5] is given by

$$\frac{\partial}{\partial t}p(\boldsymbol{x},t) = \sum_{i\in\mathcal{I}} -\boldsymbol{e}_i^T\nabla[r_i(\boldsymbol{x},t)p(\boldsymbol{x},t)] + \frac{1}{2\Omega}\boldsymbol{e}_i^T\vec{\boldsymbol{H}}(r_i(\boldsymbol{x},t)p(\boldsymbol{x},t))\boldsymbol{e}_i, \tag{3}$$

where $\Omega \gg 1$ is the system size, $\boldsymbol{x} = \boldsymbol{X}/\Omega$, $r_i = R_i/\Omega$ and $\vec{\boldsymbol{H}}$ denotes the Hessian. The probability mass $P(\boldsymbol{X},t)$ is approximated by $p(\boldsymbol{x},t)/\Omega^d$. Equation (3) is a particular form of the more general Fokker–Planck equation [16].

We may extend the class of reactions by modeling non-local state changes to describe, for example, species production in "bursts". Such a process, indexed by $j \in \mathcal{J}$, may be associated with a kernel $\mathcal{B}_j(y,t)$, describing the probability density of a state change of size $y \in \mathbb{R}$ at time t, and the rate $f_j(\boldsymbol{x},t)$, describing the rate of such changes occurring from state $\boldsymbol{x}$ at time t. The non-local model then takes the form

$$\begin{aligned}\frac{\partial}{\partial t}p(\boldsymbol{x},t) = &\sum_{i\in\mathcal{I}} -\boldsymbol{e}_i^T\nabla[r_i(\boldsymbol{x},t)p(\boldsymbol{x},t)] + \frac{1}{2\Omega}\boldsymbol{e}_i^T\vec{\boldsymbol{H}}(r_i(\boldsymbol{x},t)p(\boldsymbol{x},t))\boldsymbol{e}_i \\ &+ \sum_{j\in\mathcal{J}} -f_j(\boldsymbol{x},t)p(\boldsymbol{x},t) + \|\boldsymbol{e}_j\|\int_{\boldsymbol{x}-z\boldsymbol{e}_j\in\mathbb{R}^d_+} f_j(\boldsymbol{x}-z\boldsymbol{e}_j,t)p(\boldsymbol{x}-z\boldsymbol{e}_j)\mathcal{B}_j(z\|\boldsymbol{e}_j\|,t)\,\mathrm{d}z.\end{aligned} \tag{4}$$

This is also closely related to droplet breakup and coalescence, where the equation is called the *Smoluchowski* coagulation equation, and has been used extensively in models from aerosols to cosmological structure formation [17]. While our focus is on the breakup process rather than aggregation, this framework may be extended to incorporate an aggregation term.

Lastly, we introduce discrete states indexed by $k \in \mathcal{K}$, whereby the probability is distributed among the family of densities $\{p_k\}_{k\in\mathcal{K}}$. There is a flux of probability from state $k \in \mathcal{K}$ to state $\ell \in \mathcal{K}$ at a rate of $g_{k\ell}(\boldsymbol{x},t)$, that may depend on the continuum state and time. Importantly, all other rates (reaction and non-local) may depend on the discrete state k, and are subscripted to reflect this. In this way, we avoid having to consider reactions and non-local processes, indexed by $\mathcal{I}$ and $\mathcal{J}$, respectively, that depend on the discrete state $k \in \mathcal{K}$. Instead, we may consider $\mathcal{I}$ and $\mathcal{J}$ to include the union of all local and non-local interactions, and set the rates to zero for the appropriate $k \in \mathcal{K}$. The final form of the system is

$$\left\{\begin{aligned}\frac{\partial}{\partial t}p_k(\boldsymbol{x},t) = &\sum_{i\in\mathcal{I}} -\boldsymbol{e}_i^T\nabla[r_{ik}(\boldsymbol{x},t)p_k(\boldsymbol{x},t)] + \frac{1}{2\Omega}\boldsymbol{e}_i^T\vec{\boldsymbol{H}}(r_{ik}(\boldsymbol{x},t)p_k(\boldsymbol{x},t))\boldsymbol{e}_i \\ &+ \sum_{j\in\mathcal{J}} -f_{jk}(\boldsymbol{x},t)p_k(\boldsymbol{x},t) + \|\boldsymbol{e}_j\|\int_{\boldsymbol{x}-z\boldsymbol{e}_j\in\mathbb{R}^d_+} f_{jk}(\boldsymbol{x}-z\boldsymbol{e}_j,t)p_k(\boldsymbol{x}-z\boldsymbol{e}_j)\mathcal{B}_{jk}(z)\,\mathrm{d}z \\ &+ \sum_{\ell\in\mathcal{K}} -g_{k\ell}(\boldsymbol{x},t)p_k(\boldsymbol{x},t) + g_{\ell k}(\boldsymbol{x},t)p_\ell(\boldsymbol{x},t)\end{aligned}\right\}_{k\in\mathcal{K}}. \tag{5}$$

What do the discrete states model? Retaining a discrete description is crucial for molecules not expected to be present in large numbers. In this case, we consider d to denote the number of continuum species. The discrete states may also be used to describe abstract system states in which different behaviour governs the reaction network. For example, light-induced recombination [18] allows cells to alter their genetic structure, thereby changing the reaction network behaviour. This transition to a different governing dynamic may be encapsulated by transition between discrete states. We will demonstrate a third use-case for the discrete states: phantom states, that do not correspond to a physical configuration of the system. The phantom states allow for a broader class of auxiliary population-level dynamics to be encapsulated in the model. In light of system (5) describing chemical reactions augmented by a class of auxiliary processes, we henceforth call system (5) as the Augmented Chemical Master Equation (ACME).

While the focus of this work is the continuum setting — to allow the efficient computation of significantly larger populations than is possible in the discrete setting — we emphasise that this augmentation may be performed analogously in the discrete setting, to obtain system descriptions extending beyond the reach of classical master equation descriptions. For this reason, we refer to the conceptual framework as an Augmentation of the CME, while pursuing the current implementation on its continuum approximation.

Armed with the ACME framework of system (5), we proceed to outline the implementation of a numerical solver capable of solving system (5) in the general case, which we call the Flips solver.

2.2 The Flips library

In this section we briefly survey numerical solvers in the chemical kinetics literature to establish the context of the numerical scheme we employ. We stress that all of these solutions remain grounded within the classical CME framework, and thus fall short from the population-level perspective.

Numerical simulation of stochastic reaction networks has an extensive and richly developed literature. Rather than an exhaustive survey, we provide an outline of the approaches and their motivations and relative merits. Reaction networks are commonly modeled as a continuous-time Markov chain (CTMC) whose state distribution is governed by the CME. When the possible number of states becomes large, solving the master equation becomes prohibitively challenging. An alternative to solving the CME is to generate exact sample trajectories of the stochastic process via the Stochastic Simulation Algorithm (SSA) [19, 20]. Stochastic simulation of the underlying CTMC is equivalent to the master equation in the sense that each simulated trajectory is a sample from the distribution given by the solution of the master equation. In other words, the underlying stochastic process is identical, the CME captures the full distribution while the SSA merely samples from it. For accurate resolution of the state distribution, large number of sample paths are often required, which has lead to a rich set of refinements [21] and approximations [22]. Hybrid approaches that attempt to efficiently capture dynamics at different state [23] or time [24] scales remain a topic of active research. Ultimately, it remains challenging to produce a sufficient number of trajectories to accurately resolve the distribution.

In an attempt to avoid stochastic sampling but accelerate solution of the full CME, several model reduction approaches have been considered, such as the Finite State Projection method [25], leveraging timescale separation [26], lumping (or aggregating) states [27, and references therein], as well as various spectral approximations [28, 29]. Hybrid combinations of these techniques have also been composed [30, and references therein].

One prevalent model reduction techniques is the class of continuum approximations of the CME, in particular, the Fokker–Planck equation [15, 16]. The underlying assumption is that, when only a small number of molecules need to be simulated the computational complexity is manageable, but when species are expected to have large copy numbers, a continuum approximation is appropriate. Just as the Fokker–Planck equation is the continuum analogue of the CME, the Langevin equation is the continuum analogue of the continuous-time Markov chain. That is, the Langevin equation describes the underlying stochastic process whose distribution is captured by the Fokker–Planck equation.

Various numerical schemes for solving the Fokker–Planck approximation of the CME appear in the literature [31, 32]. Just as with the trajectory sampling, many studies adopt hybrid approaches. In [33, 34], reactions are partitioned into fast and slow, and sample paths are generated by the Langevin equation or variants of the SSA discussed above. However, the Monte Carlo sampling requires a large number of samples just as for the aforementioned discrete sampling. In [35], the dynamics for each species are partitioned depending on molecule count. A discrete description is implemented for small molecule count (where the continuum assumption breaks down), while the continuum approximation is adopted

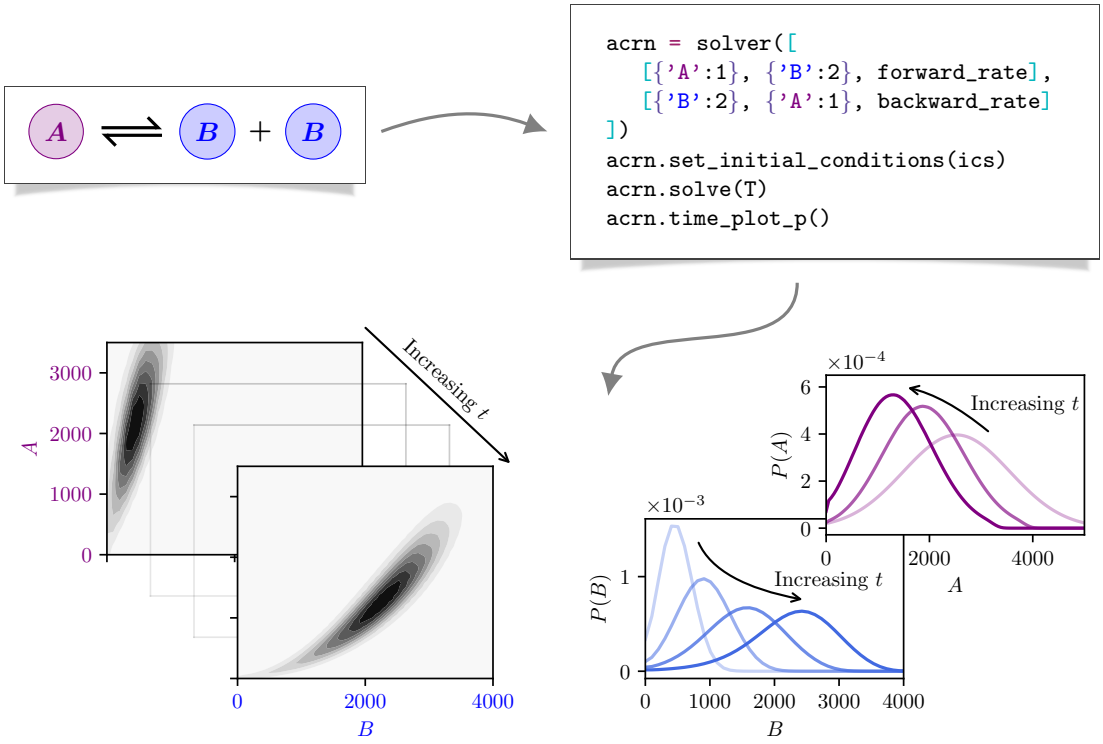

Figure 2: Schematic depiction of the Flips solver pipeline. Beginning with a (possibly augmented) chemical reaction network, we encode the reactions, set the initial distribution, and instruct the solver to determine the state distribution up to a terminal time $t = T$ or terminal event. We may then plot the evolution of the state distribution, and its marginals, over time. For the sake of clarity, at this point we illustrate a classical chemical reaction network to highlight the simple one-to-one encoding of the reaction network, and the flavour of results the solver generates. The abstract and non-physical augmentation that distinguish the ACME framework are demonstrated on more substantial networks in Section 3.

for larger numbers of molecules. In [36], species are separated into those that are expected to have only small copy numbers for which the discrete description is retained, and those expected to exist in large number where the continuum description is accurate, although non-local contributions in the continuum species are not incorporated.

As we will discuss, in the extended setting of the ACME framework, the quantity p governed by (5) does not always represent a probability distribution. Therefore, the direct link to the underlying stochastic process is severed, rendering stochastic sampling techniques not directly applicable. We instead develop a solver based on the system of differential equations (5), which we call the Flips solver (loosely acronymous of the Fokker–Planck system it is designed to solve). Species are separated into those whose description remains discrete, and those whose description are approximated on the continuum, in which we allow non-local dynamics. Most substantially, the solver is built to capture the augmentation of the classical chemical reaction structure, capable of encapsulating auxiliary population-level processes and thus appreciably expanding the model scope, as we demonstrate in the sequel.

To solve system (5) numerically, we begin by discretising the state space. Despite having d continuum-state dimensions, each continuum reaction $i \in \mathcal{I}$ in the model (5) acts only to advect and diffuse probability density in the $\boldsymbol{e}_i$ direction. Since $\boldsymbol{e}_i \in \mathbb{Z}^d$, there is a natural discretisation for an arbitrary network on uniform grids that preserves this one-dimensional structure. Similarly, each burst production changes the state by $\boldsymbol{e}_j \in \mathbb{Z}^d$ for $j \in \mathcal{J}$, and thus the non-local integral term describes an exchange of probability in the $\boldsymbol{e}_j$ direction, which is similarly preserved on the uniform grid. This observation means that the differential and integral operators act in one-dimension even in a high-dimensional system with multiple species thereby inducing no spurious diffusion in orthogonal directions.

Our approach is to adopt a uniform grid in state space, where we truncate the space at some sufficiently large boundary where we expect only negligible probability density to accumulate. For such a numerical scheme to yield computational advantage over solving the underlying discrete system (2), the

state step Δx must satisfy two competing constraints. On the one hand, $\Delta x \ll 1$ is to be sufficiently small so that the scheme is accurate, while on the other hand, it must be nominally larger than a single discrete molecule, that is, $\Delta x > 1/\Omega$, where Ω is a typical number of molecules (see the scalings below (3)). In practice, the molecule copy number is typically $\Omega \gtrsim 10^4$, while we will consider Δx on the order of $\mathcal{O}(10^{-2})$, and thus both of these constraints are well met.

The conservative finite-volume numerical scheme is presented and analysed in Appendix A. The Flips solver is made open-source [14] to encourage its use and development. We emphasise that the Flips solver has been written with two distinct types of user in mind.

First, the practitioner principally interested in simulation results with less focus on the numerical implementation details. With this in mind, the code is distributed as a package in the open-source and widely distributed Python programming language. The interface allows for a direct encoding of the reaction network structure without reference to the underling mathematical abstraction, as depicted in Fig. 2.

Second, for the user interested in more control of the numerical implementation, the interface provides options to calibrate the state discretisation and tweak the flux limiter, as well as adjust the time stepping method and its order. Furthermore, the code has been written in a modular way that allows the more advanced user to retain the framework structure and implement a completely custom discretisation with minimal effort. For example, an implementation of a first-order finite difference scheme is included in the code, and achieved in little more than 20 lines of code. Building upon this, second- and third-order extensions are achieved in little more than 10 lines of code each.

We proceed to describe case studies in which we cast problems of interest from the literature in the ACME framework and solve them using the Flips software.

3 Applications

Our aim is to combine a representation of highly non-trivial systems involving chemical reactions coupled to auxiliary processes to demonstrate how the hybrid structure of the ACME formulation of system (5) can be exploited to tackle an extensive class of problems. We benchmark the Flips solver by comparing simulations of each example problem with analytical results.

3.1 First-passage times in self-regulated gene expression

Our first example is a model of regulated protein production as described in [12, 37]. The reaction network may be written as

$$\begin{aligned} \varnothing &\xrightarrow{\text{Hill(Protein)}} \text{mRNA}, \\ \text{mRNA} &\xrightarrow{\gamma B} \text{mRNA + Protein}, \\ \text{mRNA} &\xrightarrow{\gamma} \varnothing, \\ \text{Protein} &\xrightarrow{\gamma_0} \varnothing. \end{aligned} \tag{6}$$

The system comprises transcription of mRNA molecules, translation of protein molecules, and the degradation of both species. The dynamics are self-regulated because the mRNA transcription is regulated by the quantity of protein present, inducing a feedback loop. The notation Hill$(\cdot)$ represents that the feedback is modulated by a Hill function.

As described in [12, 37], the characteristic timescale of the mRNA dynamics $1/\gamma$ is often exceeded by the protein lifetime timescale $1/\gamma_0$. In the limit as $\gamma/\gamma_0 \to \infty$, the mRNA acts instantaneously to produce a burst of proteins, and the reaction network reduces to

$$\begin{aligned} \varnothing &\xrightarrow{\text{burst(Hill(Protein),}B)} \text{Protein}, \\ \text{Protein} &\xrightarrow{\gamma_0} \varnothing, \end{aligned} \tag{7}$$

where burst$(\cdot)$ describes production in bursts at a rate Hill(Protein) of mean size B.

Thus we have two models from the literature describing a single genetic network. The finite mRNA lifetime model (6) is more general but less easy to analyse, while the infinitely fast mRNA model (7) is less general but simpler. Our aim is to use these two models as a first demonstration of how both of these reaction networks descriptions (6) and (7) may be encapsulated and studied within the ACME framework of system (5). We then turn our attention to an insightful first-passage time problem studied

for the second system (7). We describe how this problem too may be simulated and studied using the Flips solver, and significantly extend results previously reported.

Since the protein copy number is typically large, the proteins are taken on the continuum: represented by x where $d = 1$. Both studies [12, 37] neglect the stochastic noise expressed by the diffusive term of order $1/\Omega$, and thus, for the sake of comparison, we too consider the noiseless limiting case as $\Omega \to \infty$.

In system (6), the mRNA will remain discrete, and the system may be written as

$$\frac{\partial}{\partial t}p_k(x,t) = -\frac{\partial}{\partial x}[(k\gamma B - \gamma_0 x)p_k(x,t)] - (H(x) + \gamma k)p_k(x,t) + \gamma(k+1)p_{k+1}(x,t) + \mathbb{1}_{k>0}H(x)p_{k-1}(x,t), \tag{8}$$

where $\mathbb{1}_{k>0}$ denotes the indicator function, and H denotes the Hill function given by

$$H(x) = r_0 + r_1\frac{x^n}{1+x^n}. \tag{9}$$

Each discrete state k represents the number of mRNA molecules present. In practice, we truncate the discrete mRNA state at some finite maximum $0 \leq k \leq K$.

System (7) may be written as

$$\frac{\partial}{\partial t}p(x,t) = \frac{\partial}{\partial x}[\gamma_0 x p(x,t)] - H(x)p(x) + \int_0^x H(x-z)p(x-z,t)\frac{\mathrm{e}^{-z/b}}{b}\,\mathrm{d}z, \tag{10}$$

for the mean continuum-scaled burst size $b = B/\Omega$.

Both reaction networks (6) and (7) fall within the ACME framework (5), and may then be solved numerically by application to the forms (8) and (10). To demonstrate the simplicity of using the Flips software, we present the code required to setup and simulate both reaction networks in Appendix B. Most of the code is simply a one-to-one translation of the discrete reaction network (each reaction is described by its reactants, products and rate). Intuitive instructions tell the solver to ignore diffusion, fix uniform initial conditions, solve over a specified time interval, and plot the distribution. This makes the software accessible to the end-user without the need to deal with the technicalities of the continuum approximation or its analysis. At the same time, the software allows fine-grained control of the discretisation of the state space and the differential operators, as well as the time stepping method and associated properties.

For the sake of comparing to results in [37], we adopt the same parameter values, namely

$$r_0 = 2, \qquad r_1 = 10, \qquad n = 4, \qquad B = 40, \qquad \gamma_0 = 1, \qquad \Omega = 200. \tag{11}$$

First, we explore the stationary distributions of these systems by comparing them to benchmark solutions. In the case of finite mRNA lifetime, the CME (with discrete state-space) associated with (6) is solved using the Flips solver to provide the steady-state distribution of the discrete model. For infinitely fast-lived mRNA, the stationary distribution of the continuum (10), which we denote $p_\infty(x)$, is given by [37]

$$p_\infty(x) = \frac{c}{\gamma_0}\mathrm{e}^{-x/b}x^{r_0/\gamma_0 - 1}(1+x^n)^{r_1/(n\gamma_0)}, \tag{12}$$

where r_0, r_1 and n are the Hill function parameters, and c is a normalisation constant. These two distributions (black curves) are a useful comparison for the Flips solver (coloured curves) as illustrated in Fig. 3.

In Fig. 3a we plot the stationary distributions of (8) as given by the Flips solver (solid curves) and the full CME (dotted curves) for finite, increasing values of the mRNA production/degradation rate γ. The limiting case of $\gamma = \infty$ is plotted by simulation of (10) and compared to the exact continuum solution (dashed curve) given in (12). We see good agreement even though the Flips solver has lumped every ten protein molecules into a single discrete volume. Importantly, results in [37] were obtained only in the limiting case of $\gamma/\gamma_0 \to \infty$, and thus intermediate values of γ/γ_0 were beyond reach (see [37, Appendix F]). By retaining the finite lifetime of the mRNA molecules in formulation (8), the Flips software is able to match the CME over the entire range of relevant γ/γ_0 values, and we observe the convergence of the finite mRNA lifetime scheme towards the infinitely fast-lived scheme. In Fig. 3b we plot the norm of the discrepancy between the stationary distributions of these two schemes for increasing mRNA production/degradation rates γ. We observe a linear convergence of order $1/\gamma$, which provides an error estimate not previously reported.

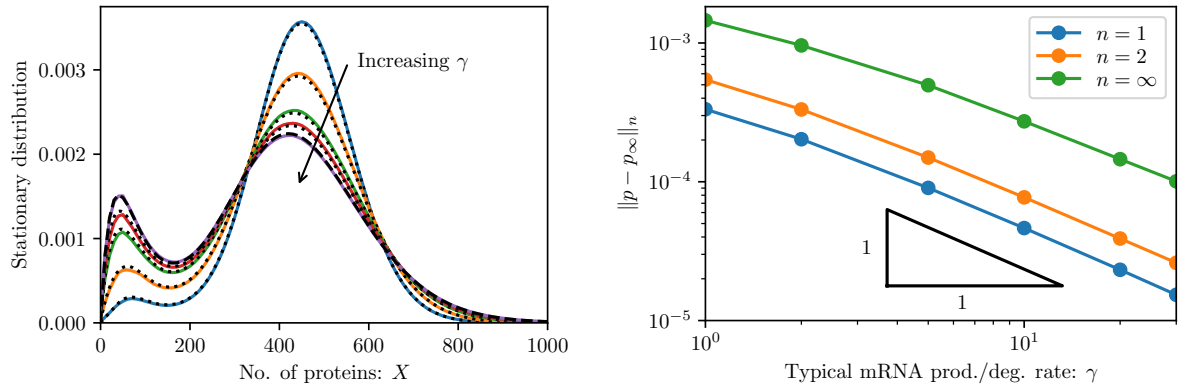

(a) $\gamma \in \{1, 2, 5, 10, \infty\}$ *(b)*

Figure 3: Comparison of the stationary distributions of two self-regulated gene expression models (6) and (7) by varying the typical mRNA production/degradation rate γ. ***(a)*** *For finite γ, the solid curves show steady-state solutions of the continuum ACME form (8) compared to dotted curves which are the steady-state solution of the associated discrete CME system, retaining $K = 30$ discrete mRNA states in both cases. For the limiting case $\gamma = \infty$, the solid curve depicts the steady-state solution of the continuum ACME form (10) compared to the dashed curve which is the exact continuum solution p_∞ in (12). All continuum simulations used $\Delta x = 0.05$, corresponding to lumping 10 discrete states together.* ***(b)*** *Convergence of the continuum ACME form (8) to the exact continuum solution p_∞ in (12) in different L^n norms. The triangle shows the $1/\gamma$ convergence rate. We employed a dicretisation of $\Delta x = 0.025$, corresponding to lumping 5 discrete states together.*

Having demonstrated the ACME framework's utility in studying model accuracy by comparing stationary distributions, we proceed to study an important transient phenomenon. One striking feature of the regulated protein production is the bimodality of the stationary distribution: the nonlinear bursting supports both a low mode and a high mode where protein production and degradation are in balance. This stationary distribution is a dynamic equilibrium: in any single cell, the stochastic expression will be continually changing the number of protein molecules. The switching between these two modes can shed light on biological event timing. Choosing an arbitrary boundary of $X_c = 165$ proteins separating the high and low protein modes, we may ask: given any initial number of proteins X, how long will it take to cross the boundary $X = X_c$, which we interpret to be a transition into the other mode. The mean switching time is given explicitly by [37]

$$T_{\text{low}\to\text{high}}(x) = \frac{1 - \gamma_0 x_c V(x_c) \mathrm{e}^{-M(x_c)}}{H(x_c)} + \int_{x_c}^{x} \mathrm{e}^{-M(y)} V(y)\, \mathrm{d}y, \tag{13a}$$

$$T_{\text{high}\to\text{low}}(x) = \int_{0}^{x} \mathrm{e}^{-M(y)} \left[V(y) - V(\infty)\right] \mathrm{d}y, \tag{13b}$$

where

$$M(x) = \log \frac{x}{H(x)} - \frac{x}{b} + \int_0^x \frac{H(y)}{\gamma_0 y}\, \mathrm{d}y, \qquad V(x) = -\int_0^x \left(\frac{1}{b\gamma_0 y} + \frac{1}{\gamma_0 y H(y)} \frac{\mathrm{d}H}{\mathrm{d}y}\right) \mathrm{e}^{M(y)}\, \mathrm{d}y. \tag{13c}$$

We would like to go beyond the mean switching time to study the full switching time distribution. Strategically leveraging the hybrid structure of the ACME framework, we may augment system (10) with an additional abstract state, so that the system is described by the densities p_0 and p_1. The original dynamics (10) are simulated on p_0, in addition to a transition to the absorbing state p_1 at a rate α, conditioned on whether the state has reached the opposite region. In other words, for an initial condition in the high-mode region $x > x_c$, the absorption rate is $\alpha \mathbb{1}_{x<x_c}$, while for an initial condition in the low-mode region $x < x_c$ the absorption rate is $\alpha \mathbb{1}_{x>x_c}$. In the limit as $\alpha \to \infty$, this models the opposite region as an immediately absorbing state. In practice, a sufficiently large value of α provides a good approximation. The switching time density is simply the probability mass that crosses the critical state x_c for the first time. With the solution of this augmented system, the switching time density is approximated by the instantaneous absorption rate.

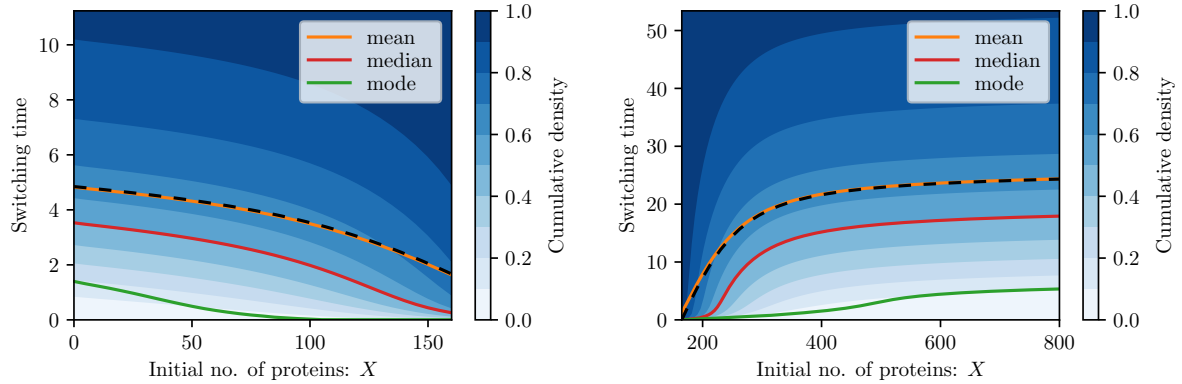

(a) $X < X_c$ *(b)* $X > X_c$

Figure 4: Switching time distribution for different initial conditions X with an absorption rate $\alpha = 1000$ and spatial discretisation of $\Delta x = 0.025$ (i.e. lumping 5 states together) up to time $t = 150$. The exact mean switching time (13), is plotted as a black dashed curve.

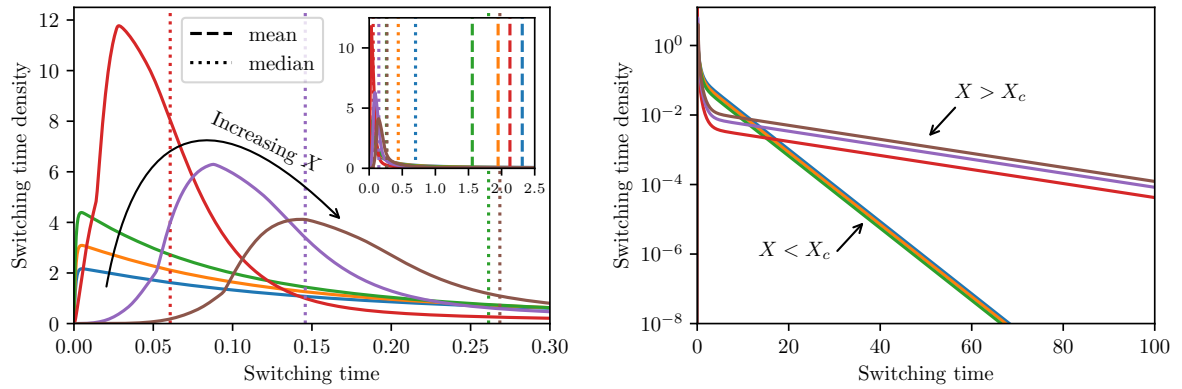

(a) *(b)*

*Figure 5: Switching time distributions, from the same data used to produce Fig. 4, with initial conditions $X \in \{140, 150, 160, 170, 180, 190\}$. **(a)** Zooming in to a small time interval resolves the modes, while **(a inset)** zooming out far enough to see the mean switching times shows the distribution skew. **(b)** The heavy tails are shown on a logarithmic scale for large times.*

In Fig. 4 we plot the cumulative switching time density, along with the mean, median and mode. The exact solution (13) is plotted as a black dashed curve, with which the numerical solution closely agrees. Strikingly, the switching time distribution is highly skewed: for an initial number of proteins $X \in (70, 450)$, the mean is at least an order of magnitude larger than the mode, and is uniformly larger than the median. It is important for both the experimentalist and theoretician to keep this heavy tail in mind: with a small number of samples, switching times near the mode (and not the mean) are likely going to dominate the sample.

We plot a selection of the switching time densities in Fig. 5, for initial conditions in both the low- and high-mode regions, to demonstrate just how far the mean is from the mode near the critical number of proteins X_c. The heavy tails of these distributions are illustrated in Fig. 5b, where we distinguish different large-time asymptotic behaviour for initial conditions below/above the critical boundary X_c. The exponential decay in the switching time density suggests that the profile p converges to a separable solution of the form $p(x,t) \sim T(t)Y(x)$ for $T(t) = \mathrm{e}^{-\lambda t}$ motivating further analytical study.

In the models of self-regulated gene expression studied in this paper, the Flips solver is able to quantify model accuracy and convergence rates. By augmenting an abstract discrete state to capture a first passage, the Flips solver is able to produce the full first-passage time distribution, revealing a remarkably rich structure of heavy-tailed distributions distinguished by the critical boundary between

the high and low modes of protein expression. We proceed to study a population-level auxiliary process that cannot be captured by a master equation, showing that careful manipulation of physical constraints make the problem tractable within the ACME framework.

3.2 Phenotypic selection

When a state-dependent auxiliary process is coupled to single-cell reaction kinetics, the ACME framework is capable of describing the population-level evolution. Many phenomena can exert state-dependent selection pressures, such as external changes to the environment or media that cause metabolic and cell-cycle changes. Our second example describes the auxiliary process of state-dependent growth augmenting single-cell dynamics. When the concentration of a particular protein is heterogeneously distributed within a population, for example, due to stochastic gene expression (see Section 3.1), the protein concentration in daughter cells may be inherited from the mother cell. If the growth process depends on protein concentration to facilitate cell-cycle stages and ultimately the rate of mitosis, the population-level effect is preferential proliferation of protein concentrations.

We begin by considering the birth–death process of a chemical species X within a single cell, governed by

$$\varnothing \quad \xrightarrow{\lambda(x)} \quad \mathrm{X} \quad \xrightarrow{\mu(x)} \quad \varnothing. \tag{14}$$

The continuum approximation of process (14) takes the form [38]

$$\frac{\partial}{\partial t}p(x,t) = -\frac{\partial}{\partial x}[(\lambda(x)-\mu(x))p(x,t)] + \frac{1}{2\Omega}\frac{\partial^2}{\partial x^2}[(\lambda(x)+\mu(x))p(x,t)]. \tag{15}$$

We now add growth at a rate that depends on the quantity of X molecules denoted by $G(x)$. The population distribution may then be modeled by adding the exponential growth rate, and normalising the distribution [8, 9], whereby the governing equation becomes

$$\begin{aligned}\frac{\partial}{\partial t}p(x,t) = &-\frac{\partial}{\partial x}[(\lambda(x)-\mu(x))p(x,t)] + \frac{1}{2\Omega}\frac{\partial^2}{\partial x^2}[(\lambda(x)+\mu(x))p(x,t)] \\ &+ G(x)p(x,t) - \left(\int_0^\infty G(z)p(z,t)\,\mathrm{d}z\right)p(x,t).\end{aligned} \tag{16}$$

It seems that only in the simplest of cases is equation (16) explicitly tractable. More worryingly, it seems that equation (16) is nonlinear and not of the general ACME form (5). We proceed to demonstrate how the nonlinear equation (16) is solved by a quantity satisfying an appropriately cast ACME equation of the generic form (5), thereby allowing us to use the Flips solver to tackle this population-level problem.

First, consider q, the solution of (16) without the nonlinear normalisation, namely

$$\frac{\partial}{\partial t}q(x,t) = -\frac{\partial}{\partial x}[(\lambda(x)-\mu(x))q(x,t)] + \frac{1}{2\Omega}\frac{\partial^2}{\partial x^2}[(\lambda(x)+\mu(x))q(x,t)] + G(x)q(x,t). \tag{17}$$

The quantity $p = q/\int_0^\infty q(x,t)\,\mathrm{d}x$ then satisfies the original nonlinear (16), and thus we have reduced the nonlinear problem (16) to the linear equation (17).

Second, note that the linear equation (17) may be cast in the general ACME form (5) by considering a phantom state, to which a transition occurs with a propensity that is the negative of the growth rate, namely,

$$\frac{\partial}{\partial t}p_0(x,t) = -\frac{\partial}{\partial x}[(\lambda(x)-\mu(x))p_0(x,t)] + \frac{1}{2\Omega}\frac{\partial^2}{\partial x^2}[(\lambda(x)+\mu(x))p_0(x,t)] - [-G(x)]p_0(x,t), \tag{18}$$

$$\frac{\partial}{\partial t}p_1(x,t) = [-G(x)]p_0(x,t). \tag{19}$$

Ultimately, the ACME form of (18) and (19) allows us to use the Flips solver to solve the nonlinear population-level equation (16).

The initial probability mass is to be distributed in p_0, while $p_1(x,0) = 0$. The new state $k = 1$ is a phantom state, in that it does not represent a physical system configuration. To see this, consider, for example, the case of a positive growth rate $G(x) > 0$ then $p_1(x,t) \leq 0$ for all time t, and therefore p_1 no longer has an interpretation as a probability density. However, this non-physicality is of no concern: p_0 solves (17), and we may safely ignore the value of the phantom state p_1.

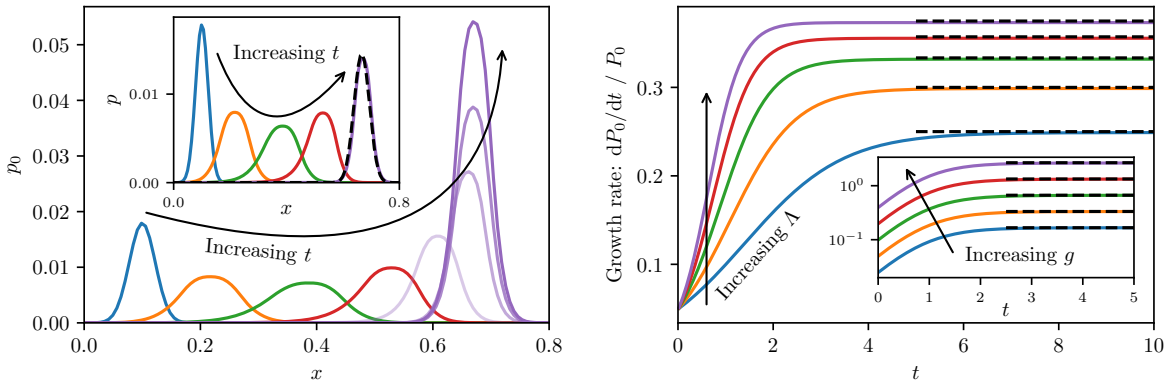

(a) *(b)*

*Figure 6: Simulations of chemical kinetics coupled to state-dependent growth (18) for $G(x) = gx$ and the birth and death functions given in (20). Initial conditions are $p_0(x, 0) = \exp(-(x - 100)^2/1000)$ and $p_1(x, 0) = 0$. **(a)** Density p_0 for growth factor $g = 0.5$ and birth factor $\Lambda = 3$ at times $t \in \{0, 0.5, 1, 1.5, 2, 3, 4, 5\}$; **(a inset)** normalised density $p = p_0/P_0$ with P_0 defined in (23) at times $t \in \{0, 0.5, 1, 1.5, 5\}$. The black dashed curve shows the asymptotic approximation of the limiting profile given by (79) in Appendix C. **(b)** Growth rate $(\mathrm{d}P_0/\mathrm{d}t)/P_0$ for grwoth factor $g = 0.5$ and birth factor $\Lambda \in \{2, 2.5, 3, 3.5, 4\}$; **(b inset)** $\Lambda = 3$ and $g \in \{0.25, 0.5, 1, 2, 4\}$. The black dashed lines show the large time predictions (80) and (83). The state space discretisation was $\Delta x = 0.007$ (i.e. lumping 7 states together).*

There are other ways of exploiting the observation that we may split the solution of (16) into a non-normalised form followed by a normalisation. For example, we could implement operator splitting: solving the non-normalised linear equation (17) and adding a normalisation at each timestep. The advantage of this approach would be that no additional discrete state need be introduced, and the numerical quantities remain $\mathcal{O}(1)$ without risk of numerical overflow at large times. When a smaller state space, or large-time simulations are crucial, this option should be considered. However, the principal advantage of our approach is that it does not require bespoke changes to the ACME framework or solver, and thus we pursue this approach for simplicity. Moreover, the quantity p_0 is a population density (as opposed to a probability density) and thus allows a direct quantification of the overall growth rate, as we now demonstrate.

For the purpose of numerical simulations, we take the underlying birth–death process studied in [38], namely

$$\lambda(x) = \Lambda x(1 - x), \qquad \mu(x) = x. \tag{20}$$

We highlight that, for $\Lambda > 1$, there is a critical point x_c for which $\lambda(x_c) = \mu(x_c)$. On $x \in (0, x_c)$, birth dominates death $\lambda(x) > \mu(x)$, and the state increases towards x_c, while for $x \in (x_c, 1)$, the opposite is true, and $\lambda(x) < \mu(x)$ and deaths dominate births driving the state down to x_c. In the vicinity of the critical point stochastic effects become important [38].

In Fig. 6a we show the solution of (18) with an initial Gaussian distribution centred at $X = 100$. The density $p_0(X, t)$ drifts toward higher values of X and from $t \approx 5$ appears to have a stationary centre point after which time the growth is evident. In the inset of Fig. 6a we plot the normalised density $p = p_0/\int_0^\infty p_0(x, t)\,\mathrm{d}x$, and find that, for large times, the profile remains largely unchanged.

Motivated by the observation that the normalised density p appears to converge for large times t, we seek a separable solution of equation (17). The calculations are detailed in Appendix C where we deduce that the profile tends to

$$p_0(x, t) \sim T(t)Y(x), \tag{21a}$$

where

$$T(t) = \mathrm{e}^{r_0 t}, \qquad Y(x) = \frac{1}{\sqrt{a\Omega\pi}}\mathrm{e}^{-(x-x_c)^2/(a\Omega)}, \tag{21b}$$

The limiting profile (21) is a Gaussian centred at $x = x_c$ of width $\mathcal{O}(1/\sqrt{a\Omega})$ growing at rate r_0, which is given by

$$r_0 = G(x_c). \tag{22}$$

For $G(x) = gx$, as used in our simulations, this becomes $r_0 = g(1 - 1/\Lambda)$.

These calculations serve as a useful gauge for our numerical simulations as illustrated in Fig. 6. In the inset of Fig. 6a we show the limiting normalised density (21), and observe good agreement with the numerical simulation at $t = 5$. We define the average growth rate of the numerical solution by $(\mathrm{d}P_0/\mathrm{d}t)/P_0$, where P_0 denotes the total density in the $k = 0$ state, that is,

$$P_0 = \int_0^\infty p_0(x,t)\,\mathrm{d}x. \tag{23}$$

In Fig. 6b we plot the average growth rate, and the predicted limiting growth rate (22) as black dashed lines, to which the numerical simulations converge for a range of system parameters.

To recap, the augmented reaction network considered in this section is not strictly physical, as we incorporated negative propensities that induce negative "probabilities". Nevertheless, by carefully crafting such a non-physical network, we were able to couple the single-cell reaction kinetics with an auxiliary growth process while taming the associated nonlinearity. In fact, the numerical simulations motivated the analytical study, which in turn uncovered insightful analytical information regarding the modes and long-time behaviour of the system, and allowed us to validate the simulations. We now turn our attention to an auxiliary fragmentation process that demonstrates the extensive coverage of the ACME framework.

3.3 Divide and fragment

Our final example does not stem from a classical chemical reaction network, but a growth–fragmentation process. For an accessible introductory treatment, we refer the reader to [11, ch. 4]. In this class of models, the independent state variable x typically represents size, and we distinguish the density from the previous densities by denoting it $\rho(x,t)$, with the volume density given by $x\rho(x,t)$. It is instructive to have in mind the concrete example of cell growth and mitosis, and we will adopt the corresponding nomenclature, while keeping in mind that the models may be applied significantly more broadly as discussed in Section 2.1.

The number density ρ is governed by the equation

$$\frac{\partial}{\partial t}\rho(x,t) = -\frac{\partial}{\partial x}[g(x,t)\rho(x,t)] - B(x,t)\rho(x,t) + \int_x^\infty b(y,x,t)\rho(y,t)\,\mathrm{d}y. \tag{24}$$

The first term on the right-hand side of (24) represents the growth at a rate $g(x,t)$. The final two terms represent the fragmentation. The first of these terms describes the reduction of cells of size x due to fragmentation, where $B(x,t)$ is the rate of fragmentation of cells of size x. The integral term adds all the cells $y > x$ that fragment into cells of size x, where $b(y,x,t)$ is the fragmentation rate per unit size of cells of size y that fragment into a piece of size x and another piece of size $y - x$.

A no-flux boundary condition is imposed at $x = 0$, with the flux given by $g(x,t)\rho(x,t)$, and a (sufficiently rapid) vanishing far-field condition as $x \to \infty$. The model is typically studied in the absence of diffusion.

As we demonstrate in Appendix D, the model accounts for the fragmentation splitting one cell into several while conserving volume by imposing constraints on B. In Appendix D we further show how the representation in equation (24) can be transformed to a rate and kernel, equivalent to the burst production process and conforming to the ACME structure of system (5). Thus, despite not being a chemical reaction network, the growth–fragmentation process is solvable with the Flips software. Two key properties of the system are that the rate of change of number and volume densities are governed by the average fragmentation and growth, respectively, that is,

$$\frac{\mathrm{d}}{\mathrm{d}t}\int_0^\infty \rho(x,t)\,\mathrm{d}x = \int_0^\infty B(x,t)\rho(x,t)\,\mathrm{d}x, \qquad \frac{\mathrm{d}}{\mathrm{d}t}\int_0^\infty x\rho(x,t)\,\mathrm{d}x = \int_0^\infty g(x,t)\rho(x,t)\,\mathrm{d}x. \tag{25}$$

Equations (25) are derived in Appendix D.

We now seek a benchmark case with which we can compare numerical solutions. In Appendix E we combine results from [39] and [40] to derive two closed-form solutions for two growth–fragmentation

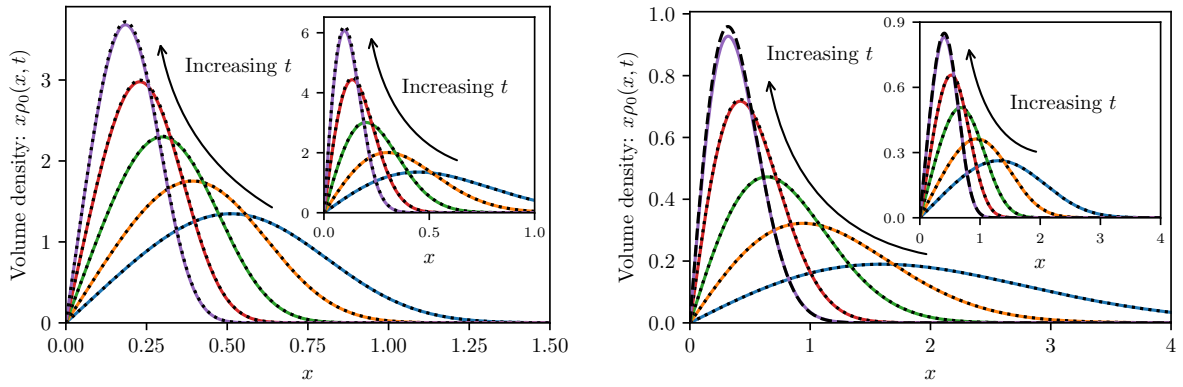

*Figure 7: Analytical (black dotted curves) and numerical (coloured curves) solutions of growth–fragmentation equations at various times t. **(a)** Equation (26) with solution (27) at times $t - t_0 \in \{0, 0.6, 2, 5, 10\}$ where $t_0 = 0.5$ and $k = 3$; **(a inset)** $k = 2$; **(b)** Equation (28) with solution (29) at times $t - t_0 \in \{0.04, 0.12, 0.4, 2\}$ where $t_0 = 0.02$ and $k = 2$; **(b inset)** $t - t_0 \in \{0.017, 0.07, 0.2, 2\}$ where $t_0 = 0.01$ and $k = 3$. The black dashed curves in (b) show the limiting profile as $t \to \infty$ given by (30). Other parameters used are $a = 5$, $\Delta x = 0.005$. Initial conditions are given by the analytical solution at time $t = t_0$.*

equations. In the first case, we use the time-invariant fragmentation kernel $b(y, x, t) = 2ay^{k-1}$ for positive constants a and k, with no growth, that is, $g \equiv 0$. The equation takes the form

$$\frac{\partial}{\partial t}\rho(x,t) = -ax^k\rho(x,t) + \int_x^\infty 2ay^{k-1}\rho(y,t)\,\mathrm{d}y, \tag{26}$$

and admits the self-similar solution

$$\rho(x,t) = c(at)^{2/k}\mathrm{e}^{-atx^k}, \tag{27}$$

for an arbitrary constant c. A change of variables (see Appendix E) allows us to transform (27) to a solution of the equation

$$\frac{\partial}{\partial t}\rho(x,t) = -\frac{\partial}{\partial x}\left[x\rho(x,t)\right] - (akx^k + 1)\rho(x,t) + \int_x^\infty 2aky^{k-1}\rho(y,t)\,\mathrm{d}y, \tag{28}$$

which is given by

$$\rho(x,t) = c\,\mathrm{e}^{-2t}[a(\mathrm{e}^{kt} - 1)]^{2/k}\mathrm{e}^{-a(\mathrm{e}^{kt}-1)(\mathrm{e}^{-t}x)^k}. \tag{29}$$

Equation (28) describes growth linear in size, $g(x,t) = x$, and uniform decay.

Physically, the first example (26) describes a pure fragmentation process where the probability of a cell of size y being divided into cells of size x and $y - x$ is uniform for all $0 \le x \le y$. Thus, we expect the solution (27) to concentrate an increasing (and diverging) number density in a vicinity of the origin. Indeed, we see that, for any positive x, $\rho(x,t) \to 0$ while $\rho(0,t) \to \infty$ as $t \to \infty$. The volume density, $x\rho(x,t)$, while eventually vanishing at every point x, conserves its integral, as per (25), and this is what we illustrate in the simulation plots.

The second example (28) incorporates growth and decay, acting in competition with the fragmentation. How these competing forces balance in asymptotically large time is not trivial. We find that, in the limit as $t \to \infty$, the density ρ from (29) converges to the profile

$$\rho(x,t) \sim ca^{2/k}\mathrm{e}^{-ax^k}. \tag{30}$$

We model equation (26) by considering a species X undergoing a non-local fragmentation with kernel $b(y,x) = ay^{k-1}$. This corresponds to a fragmentation rate of ax^k and a uniform fragmentation distribution (see Appendix D). Equation (28) requires two extra ingredients: production of X (in the sense of a

reaction network, which captures growth in growth–fragmentation processes) and exponential transition to a new discrete state (decay). The species X is produced by a reaction at a rate proportional to its quantity

$$\varnothing \xrightarrow{X} X, \tag{31}$$

in the diffusion-free limit $\Omega \to \infty$. Adding a discrete state allows us to incorporate the decay term, ultimately arriving at the system

$$\frac{\partial}{\partial t}\rho_0(x,t) = -\frac{\partial}{\partial x}[x\rho_0(x,t)] + \int_x^\infty 2ax^k\rho_0(y,t)\,\mathrm{d}y - ax^k\rho_0(x,t) - \rho_0(x,t), \tag{32}$$

$$\frac{\partial}{\partial t}\rho_1(x,t) = \rho_1(x,t). \tag{33}$$

For both examples, we use the initial condition given by the analytical solution at a nominal time $t = t_0$, that is, $\rho_0(x,0) = \rho(x,t_0)$.

In Fig. 7 we illustrate the analytical (black dotted curves) and numerical (coloured curves) solutions of equations (26) and (28) for $a = 5$ and $k = 2, 3$ at different times t. In Fig. 7a, we simulate equation (26) describing only fragmentation, which manifests as the volume density becoming concentrated around smaller sizes (near the origin). In contrast, Fig. 7b shows simulations of equation (28), where fragmentation acts in combination with decay to diminish the total volume density, and in competition with linear growth. The numerical solutions exhibit good agreement with the analytical solution. In equation (28), the growth, decay, and fragmentation balance at asymptotically large time and the process converges toward the stationary distribution profile (30) as a black dashed curve in Fig. 7b. We see that the long-time asymptotics are well approximated by the numerical solution already by time $t = 2$.

We have pointed out that both the dependent and independent quantities in the growth–fragmentation model (24) differ conceptually from their counterparts in the general reaction network model (5). Nonetheless, the model is of the same general form, and thus the solver is no less applicable. This is a powerful observation, since it allows us to couple these two classes of models. This is applicable to cell cycle modeling, where fragmentation (describing mitosis) depends on gene expression pathways [41, 42, 43], as well as other biochemical processes [10]. The ACME framework in tandem with the Flips software provides a generic framework in which such coupled models can be studied, alongside population-level effects and with view to transient dynamics (such as first-passage time problems).

4 Conclusions

The aim of this work is to establish a unifying framework for auxiliary processes coupled to arbitrary internal reaction kinetics that extend beyond classical chemical master equation descriptions. The Augmented Chemical Master Equation (ACME) framework that we introduce, is grounded in the classical CME. Considering the prohibitive challenge of solving the CME for large copy numbers, we take the Fokker–Planck continuum approximation for species that are typically large, while retaining discrete states for the remaining species. For the continuum states, we capture non-local effects, such as production in bursts.

We may leverage the discrete states to describe abstract system configurations that are not simply cardinal quantities, for example, binding/unbinding events, cell-fate decisions, and so forth. We demonstrate this use in modeling transient dynamics of self-regulated gene expression to solve the first-passage time problem (Section 3.1). The method provides the complete first-passage time distribution of the bimodal system, extending previous results in the literature.

Another use for the discrete states is to describe non-physical phantom system configurations. The power of this approach is that it allows the underlying equations to capture dynamics beyond the reach of the classical chemical master equation. We demonstrate this by simulating population-level phenotypic selection (Section 3.2). Typically a nonlinear problem, we prove that the nonlinear component may be resolved separately by normalising the solution of a master equation with an exponential growth term, thereby reducing the problem to a linear one. The growth is captured by transition to a phantom state at a (non-physical) negative rate. The phantom state has no physical interpretation (with negative "probabilities"), but its presence makes the extended population-level dynamics tractable within the unified ACME framework, and thus directly solvable with the Flips solver.

Finally, the general problem tackled within the ACME framework is applicable to equations not typically associated with the chemical master equation, such as growth–fragmentation models (Section 3.3).

We demonstrate that the Flips solver provides an accurate tool for this class of models, and point to physical phenomena described by growth–fragmentation which are coupled to processes classically modeled with the master equation. This hints at further benefits of coupling the master equation to such auxiliary processes, motivating future work in this direction.

All of the results were obtained by casting the diverse collection of examples in the ACME framework, and solving these using the Flips solver. The run-time of each simulation depends strongly on the time and space discretisation. The time-step is typically dependent on both the space step as well as the specific problem structure and parameters (see (62) in Appendix A). The examples presented here typically took between a couple of seconds and a couple of minutes on a single core of a standard laptop computer.

Certain limitations exist in the current formulation. While the ACME framework may be extended straightforwardly to incorporate non-local aggregation, the Flips solver is not currently designed to calculate a quadratic form in the integrand. The population-level dynamics (for example, the growth rates) are implicitly assumed to be deterministic. Since our primary focus has been on population-level dynamics acting on species modeled in the continuum, this assumption seems fitting, however, the more general setting requires an appreciably more involved formulation.

The hybrid network structure combining the continuum and discrete descriptions, alongside non-local dynamics, applied in versatile, often non-physical, ways, such as the use of negative reaction rates, significantly extends the scope of the classical master equation formulation. Our hope is that this augmented approach, and the accompanying software, puts a richer class of models and complex coupled processes firmly within reach.

Appendix

A Numerical solver

In this Appendix, we detail the numerical scheme employed to solve system (5) and prove a result necessary for its stability.

We begin by introducing relevant notation. The fixed state scale is denoted by Δx, whereby the uniform grid is $\{0, N_1\Delta x\} \times \cdots \times \{0, N_d\Delta x\}$. We index the numerical scheme by integer vectors, where $\boldsymbol{j}\Delta x = (j_1\Delta x, \ldots, j_d\Delta x)$, and write the discrete probability mass as $(p_k)^n_{\boldsymbol{j}} = p_k(\boldsymbol{j}\Delta x, t^n)$, for a sequence of time steps $\{t^1, \ldots, t^n\}$. We similarly use the $\boldsymbol{j}$ subscript to denote evaluation of any function at the point $\boldsymbol{x} = \boldsymbol{j}\Delta x$.

The first-order differential operator describing the drift is one of the trickiest parts of the numerical implementation. We proceed to describe the finite-volume scheme used to discretise the differential operator, followed by the discretisation of the integral operator for a burst kernel. The discrete transitions are added to the explicit scheme in the classical manner. By summing over $k \in \mathcal{K}$ in (5), one finds that the discrete transitions conserve probability mass.

A.1 Finite volume scheme

We employ the second-order, central, flux-limited finite-volume scheme introduced in [44] applied for each reaction $i \in \mathcal{I}$ one-dimensionally in the $\boldsymbol{e}_i$ direction. For the sake of concreteness, we demonstrate the scheme for a system comprising a single reaction in the direction $\boldsymbol{e}$ with rate r and no non-local effects or additional discrete states, which we write as

$$\frac{\partial}{\partial t}p(\boldsymbol{x},t) = -\frac{\partial}{\partial \boldsymbol{e}}\left[r(\boldsymbol{x},t)p(\boldsymbol{x},t)\right] + \frac{1}{2\Omega}\frac{\partial^2}{\partial \boldsymbol{e}^2}\left[r(\boldsymbol{x},t)p(\boldsymbol{x},t)\right]. \tag{34}$$

The directional derivative highlights the one-dimensional nature of the differential terms. We write the scheme in a semi-discrete manner: we discretise the state operators while leaving the time derivative on the left-hand side to be dealt with by a separate time-marching scheme, namely an explicit Runge–Kutta method (or multi-level method) as discussed in [44]. The scheme has the form

$$\begin{aligned}\frac{\partial}{\partial t}p_{\boldsymbol{j}}(t) = &-\frac{1}{\Delta x}\left[r_{\boldsymbol{j}}(t)\left(p_{\boldsymbol{j}}(t) + (\nabla_{\boldsymbol{e}}p)_{\boldsymbol{j}}(t)\frac{\Delta x}{2}\right) - r_{\boldsymbol{j}-\boldsymbol{e}}(t)\left(p_{\boldsymbol{j}-\boldsymbol{e}}(t) + (\nabla_{\boldsymbol{e}}p)_{\boldsymbol{j}-\boldsymbol{e}}(t)\frac{\Delta x}{2}\right)\right] \\ &+ \frac{1}{2\Omega(\Delta x)^2}\left[r_{\boldsymbol{j}}(t)p_{j+e}(t) - 2r_{\boldsymbol{j}}(t)p_{\boldsymbol{j}}(t) + r_{\boldsymbol{j}}(t)p_{\boldsymbol{j}-\boldsymbol{e}}\right],\end{aligned} \tag{35a}$$

where

$$(\nabla_{\boldsymbol{e}} p)_{\boldsymbol{j}} = \operatorname{minmod}\left(\theta \frac{p_{\boldsymbol{j}} - p_{\boldsymbol{j}-\boldsymbol{e}}}{\Delta x}, \frac{p_{\boldsymbol{j}+\boldsymbol{e}} - p_{\boldsymbol{j}-\boldsymbol{e}}}{2\Delta x}, \theta \frac{p_{\boldsymbol{j}+\boldsymbol{e}} - p_{\boldsymbol{j}}}{\Delta x}\right), \tag{35b}$$

for

$$\operatorname{minmod}(a,b) = \frac{1}{2}(\operatorname{sgn}(a) + \operatorname{sgn}(b)) \min(|a|,|b|), \quad \text{and} \quad \operatorname{minmod}(a,b,c) = \operatorname{minmod}(\operatorname{minmod}(a,b),c). \tag{35c}$$

The parameter $\theta \in [1,2]$ influences the nature of the flux limiter: interpolating between a less oscillatory scheme ($\theta = 1$) and a less dissipative scheme ($\theta = 2$). In all the examples presented here we fix $\theta = 1$, but refer the reader to [44] and references therein for further discussion. Zero normal flux at the boundaries (for each reaction) ensures conservation, and is achieved by neglecting flux terms whose support would extend beyond the grid.

For the conservation equations studied in [44], a sufficiently small time step Δt^n obeying the CFL condition derived in [44], the scheme is monotonic and satisfies a maximum principle whereby the ℓ^∞-norm of the discrete values is non-increasing (see Theorem 5.1, Corollaries 5.1 and 5.2 in [44]).

The setting of conservation equations is more restrictive than our model (5), since we incorporate diffusion, non-local effects, discrete transitions, as well as state-dependent flux functions. Therefore, the associated CFL condition is not directly applicable. Moreover, we cannot expect to obtain a maximum principle, since the continuum dynamics do not respect a maximum principle: consider, for example, any reaction network whose stationary distribution is not uniform, and take initial conditions more spread than the stationary distribution. Nonetheless, the proof of Theorem 5.1 in [44] is adapted in Appendix A.3 to account for these additional contributions to provide a montonicity condition: for a small enough time step Δt^n, the monotonicity condition is satisfied, which ensures that artificial oscillations will not be introduced into the numerical solution.

A.2 Discretising the burst operator

The non-local contributions on the second line of (5) are made up of probability mass lost to non-local effects, and the integral term describing mass gained due to these effects emanating from other states and coming into $\boldsymbol{x}$. In this section, we describe the discretisation for the class of non-local kernels describing production in bursts. A discussion on the discretisation of fragmentation kernels appears in Appendix E, which builds on the present analysis.

To simplify the notation, we consider a single bursting process, and thus remove the subscripts j and k, taking

$$\frac{\partial}{\partial t} p(\boldsymbol{x},t) = -f(\boldsymbol{x},t)p(\boldsymbol{x},t) + \|\boldsymbol{e}\| \int_{\boldsymbol{x}-z\boldsymbol{e}\in\mathbb{R}^d_+} f(\boldsymbol{x}-z\boldsymbol{e},t)p(\boldsymbol{x}-z\boldsymbol{e})\mathcal{B}(z)\,\mathrm{d}z. \tag{36}$$

Burst kernels take the form

$$\mathcal{B}(y) = \begin{cases} \dfrac{\mathrm{e}^{-y/b}}{b}, & y > 0, \\ 0, & y < 0, \end{cases} \tag{37}$$

where b is the mean burst size, and the burst kernel has an unbounded support. On the truncated state space, we respect the finite boundary by retaining only those bursts that transfer probability mass between two states within the finite domain. This amounts to changing the domain of integration to $\boldsymbol{x} - z\boldsymbol{e} \in [0, N_1\Delta x] \times \cdots [0, N_d \Delta x]$. To ensure conservation, we must account for the corresponding reduction in mass loss. This is achieved in our scheme by focusing on the bursts emanating *from* each $\boldsymbol{x}$ (as opposed to the integral representation in (36), which describes the bursts *into* the state $\boldsymbol{x}$). For each $\boldsymbol{j}\Delta x$ on the grid, we find the largest burst that remains within the domain:

$$m_{\max} = \max_m \{m \mid \boldsymbol{j} + m\boldsymbol{e} \in [0, N_1] \times \cdots \times [0, N_d]\}. \tag{38}$$

The scheme ensures that mass is lost and gained equally. The losses

$$\frac{\partial}{\partial t} p_{\boldsymbol{j}}(t) = \sum_{m=1}^{m_{\max}} -f_{\boldsymbol{j}}(t)\mathbb{P}_m + (\text{other contributions}), \tag{39}$$

are balanced by the gains: for all $1 \leq m \leq m_{\max}$

$$\frac{\partial}{\partial t} p_{\boldsymbol{j}+m\boldsymbol{e}}(t) = f_{\boldsymbol{j}}(t)\mathbb{P}_m + (\text{other contributions}), \tag{40}$$

where we have denoted the probability of a jump of $m\boldsymbol{e}$ grid points by $\mathbb{P}_m$.

To determine the jump probability $\mathbb{P}_m$, we recall that in the finite-volume framework, the value at a point represents the probability mass of a cell around at that point. Retaining a one-dimensional projection,

$$p_{\boldsymbol{j}}(t) \approx \int_{-\Delta x\|\boldsymbol{e}\|/2}^{\Delta x\|\boldsymbol{e}\|/2} p(\boldsymbol{j}\Delta x + y\boldsymbol{e}/\|\boldsymbol{e}\|, t)\,\mathrm{d}y. \tag{41}$$

The probability to burst into a cell $m\boldsymbol{e}$ units away, is given by

$$\mathbb{P}_m = \frac{1}{\Delta x\|\boldsymbol{e}\|} \int_{-\Delta x\|\boldsymbol{e}\|/2}^{\Delta x\|\boldsymbol{e}\|/2} \int_{(m-1/2)\Delta x\|\boldsymbol{e}\|}^{(m+1/2)\Delta x\|\boldsymbol{e}\|} \mathcal{B}(y)\,\mathrm{d}y\,\mathrm{d}x, \tag{42}$$

where we assume a uniform distribution in the cell of origin. For jump kernels of the form (37), this probability may be calculated analytically, namely

$$\mathbb{P}_m = \frac{b}{\Delta x\|\boldsymbol{e}\|} q^{m-1}(1-q)^2, \qquad \text{where} \qquad q := \mathrm{e}^{-\Delta x\|\boldsymbol{e}\|/b}. \tag{43}$$

This discretisation preserves the mean burst size (on an infinite domain). To see this, note that the mean burst size may be calculated via

$$\mathbb{E}[\text{jump size}] = \Delta x\|\boldsymbol{e}\| \sum_{m=1}^{\infty} m\mathbb{P}_m = b\frac{(1-q)^2}{q} \sum_{m=1}^{\infty} mq^m. \tag{44}$$

Since $q < 1$, we may evaluate the series via

$$\sum_{m=1}^{\infty} mq^m = q\sum_{m=1}^{\infty} mq^{m-1} = q\frac{\mathrm{d}}{\mathrm{d}q}\sum_{m=1}^{\infty} q^m = q\frac{\mathrm{d}}{\mathrm{d}q}\left(\frac{1}{1-q}\right) = \frac{q}{(1-q)^2}. \tag{45}$$

From (44) and (45) it follows that

$$\mathbb{E}[\text{jump size}] = b. \tag{46}$$

Equipped with our numerical implementation, in the following section we present three examples demonstrating the use of the Flips solver and comparing the numerical results to analytical calculations.

A.3 Monotonicity condition

In this appendix, we outline the proof in [44] that the numerical scheme satisfies a maximum principle, and show how the argument may be adapted to system (5). The equation under consideration is

$$\frac{\partial}{\partial t} p(x,t) = -\frac{\partial}{\partial x}[F(p(x,t))]. \tag{47}$$

where $x \in \mathbb{R}$ is a scalar. We denote the values of the numerical scheme at time step n by $p_{\boldsymbol{j}}^n$, where $\boldsymbol{j}$ indexes the finite volume. The CFL condition is

$$\frac{\Delta t^n}{\Delta x}\|F'\|_\infty \leq \frac{1}{8}, \tag{48}$$

where Δt^n denotes the size of the nth time step, and Δx denotes the step size in state space. From Theorem 5.1 in [44] it holds that, if the CFL condition (48) is satisfied, then the ℓ^∞-norm of the scheme is non-increasing with a first-order Euler time step, that is,

$$\max_{\boldsymbol{j}} p_{\boldsymbol{j}}^{n+1} \leq \max_{\boldsymbol{j}} p_{\boldsymbol{j}}^n. \tag{49}$$

Corollaries 5.1 and 5.2 extend this result to higher-order time-stepping methods.

Our first observation is that, in preserving a uniform grid, the advection and diffusion operators may be projected onto one dimension, while the CFL condition (48) was derived for two-dimensional advection. Restriction to one dimension allows us to relax the CFL condition (48) by a factor of 2. To understand this, we highlight that the proof expresses the explicit Euler time step as

$$p_{\boldsymbol{j}}^{n+1} = p_{\boldsymbol{j}}^n + \Delta t^n \left\{ \sum_{i=1}^{d} \sum_{k=1}^{4} \alpha_{i,k} C_{i,k}(\{p_{\boldsymbol{j}}^n\}_{\boldsymbol{j}}) \right\}, \tag{50}$$

where $C_{i,k}$ are functions satisfying a local maximum principle. The discretisation admits a decomposition of the $p_{\boldsymbol{j}}^n$ contribution of the form

$$p_{\boldsymbol{j}}^n = \sum_{i=1}^{d} \frac{C_{i,3}(\{p_{\boldsymbol{j}}^n\}_{\boldsymbol{j}}) + C_{i,4}(\{p_{\boldsymbol{j}}^n\}_{\boldsymbol{j}})}{2d}, \tag{51}$$

which allows the right-hand side of (50) to be expressed as a linear combination of $C_{i,k}$ terms. The goal is to prove that the right-hand side may be expressed as a *convex* combination of $C_{i,k}$ terms, that is, where the coefficient of each $C_{i,k}$ term is positive and the sum of all coefficients is one. It may be seen from the formulae for the coefficients shown in [44] that they sum to one, and we focus on demonstrating their positivity. For each dimension i, it may be shown that $\alpha_{i,1}$ and $\alpha_{i,2}$ are non-negative by construction of the scheme, while the other two terms are bounded by

$$|\alpha_{i,k}| \leq \frac{2\|F'\|_\infty}{\Delta x}, \qquad \text{for} \qquad k = 3, 4. \tag{52}$$

With no control over the sign of these $\alpha_{i,k}$ terms for $k = 3, 4$, we may guarantee that the coefficients remain positive by choosing Δt^n small enough to ensure that the $p_{\boldsymbol{j}}^n$ contribution dominates the (possibly) negative contribution via

$$2\frac{\Delta t^n}{\Delta x}\|F'\|_\infty \leq \frac{1}{2d}. \tag{53}$$

From (53) we see that the original CFL condition (48) from [44] may be relaxed by a factor of 2, even when system (5) is multidimensional, since the differential operators act on a single dimension, that is, d is effectively one in our discretisation.

We may extend the equation under consideration to incorporate the time- and state-varying fluxes, discrete states, and non-local effects described in system (5). In this general case, we cannot hope to obtain a maximum principle since the flux function variations in state can act to concentrate probability mass, while discrete transition rates may be negative resulting in exponential growth (see Section 3.2). Therefore, the continuous dynamics do not respect a maximum principle. Instead, we focus on monotonicity. A scheme is called monotonic if it may be expressed in the form

$$p_{\boldsymbol{j}}^{n+1} = \sum_{\boldsymbol{j}} \alpha_{\boldsymbol{j}}^n p_{\boldsymbol{j}}^n, \qquad \text{for} \qquad \alpha_{\boldsymbol{j}}^n \geq 0. \tag{54}$$

Artificial oscillations driving numerical instability may result from insufficiently small time steps which violate scheme monotonicity. In analogy with the previous argument, our aim is to express the explicit Euler scheme in a form akin to (50), and find a time step Δt^n small enough to guarantee that the coefficients of $C_{i,k}$ remain positive. This suffices to guarantee monotonicity since the local maximum principle satisfied by the $C_{i,k}$ terms guarantees that these terms may be expressed as convex combinations of local $p_{\boldsymbol{j}}^n$ terms.

Neglecting terms that are inhomogeneous in the discretised system (such as the integral terms whose non-local contributions come from states of index $\hat{j} \neq j$ and sources from discrete states of index $\hat{k} \neq k$), we rewrite (5) as

$$\frac{\partial}{\partial t} p_k(\boldsymbol{x}, t) = -h_k(\boldsymbol{x}, t) p_k(\boldsymbol{x}, t) + \sum_{i \in \mathcal{I}} -\frac{\partial}{\partial \boldsymbol{e}_i} \left[r_{ik}(\boldsymbol{x}, t) p_k(\boldsymbol{x}, t) \right] + \frac{1}{2\Omega} \frac{\partial^2}{\partial \boldsymbol{e}_i^2} \left[r_{ik}(\boldsymbol{x}, t) p_k(\boldsymbol{x}, t) \right] + (\text{source terms}), \tag{55}$$

where we write the differential operators using directional derivatives to emphasise their one-dimensional nature, and the rate h_k encapsulates the homogeneous contributions of discrete transitions and non-local

effects, namely

$$h_k(\boldsymbol{x},t) = \sum_{j\in\mathcal{J}} f_{jk}(\boldsymbol{x},t) + \sum_{\ell\in\mathcal{K}} g_{k\ell}(\boldsymbol{x},t). \tag{56}$$

Focusing on a single value of k, we henceforth drop the subscript (but recycle the index k for separate use). The explicit Euler scheme may be written as

$$p_{\boldsymbol{j}}^{n+1} = p_{\boldsymbol{j}}^n + \Delta t^n \left\{ -h_{\boldsymbol{j}}^n p_{\boldsymbol{j}}^n + \sum_{i\in\mathcal{I}} \left[\frac{1}{2\Omega(\Delta x)^2} \left[(r_i p)_{\boldsymbol{j}+\boldsymbol{e}_i}^n - 2(r_i p)_{\boldsymbol{j}}^n + (r_i p)_{\boldsymbol{j}-\boldsymbol{e}_i}^n \right] + \sum_{k=1}^{4} \alpha_{i,k} C_{i,k}(\{p_{\boldsymbol{j}}^n\}_{\boldsymbol{j}}) \right] \right\} + (\text{source terms}). \tag{57}$$

The coefficients $\alpha_{i,1}$ and $\alpha_{i,2}$ are non-negative, while the remaining coefficients are bounded via

$$|\alpha_{i,k}| \le \frac{2\|r_i\|_\infty}{\Delta x}, \qquad \text{for} \qquad k = 3, 4. \tag{58}$$

Collecting terms of $p_{\boldsymbol{j}}^n$, we see that

$$p_{\boldsymbol{j}}^{n+1} = p_{\boldsymbol{j}}^n \left(1 - \Delta t^n h_{\boldsymbol{j}}^n - \sum_{i\in\mathcal{I}} \frac{\Delta t^n (r_i)_{\boldsymbol{j}}^n}{\Omega(\Delta x)^2} \right) + \Delta t^n \sum_{i\in\mathcal{I}} \left(\alpha_{i,3} C_{i,3}(\{p_{\boldsymbol{j}}^n\}_{\boldsymbol{j}}) + \alpha_{i,4} C_{i,4}(\{p_{\boldsymbol{j}}^n\}_{\boldsymbol{j}}) \right) + \sum_{\boldsymbol{j}} \beta_{\boldsymbol{j}} p_{\boldsymbol{j}}^n + (\text{source terms}), \tag{59}$$

for non-negative constants $\beta_{\boldsymbol{j}} \ge 0$. Decomposing $p_{\boldsymbol{j}}^n$ in analogy to (51), via

$$p_{\boldsymbol{j}}^n = \sum_{i\in\mathcal{I}} \frac{C_{i,3}(\{p_{\boldsymbol{j}}^n\}_{\boldsymbol{j}}) + C_{i,4}(\{p_{\boldsymbol{j}}^n\}_{\boldsymbol{j}})}{2|\mathcal{I}|}, \tag{60}$$

we may write

$$p_{\boldsymbol{j}}^{n+1} = \sum_{\boldsymbol{j}} \beta_{\boldsymbol{j}} p_{\boldsymbol{j}}^n + (\text{source terms}) + \sum_{i\in\mathcal{I}} \left[\frac{1}{2|\mathcal{I}|} \left(1 - \Delta t^n h_{\boldsymbol{j}}^n - \sum_{i\in\mathcal{I}} \frac{\Delta t^n (r_i)_{\boldsymbol{j}}^n}{\Omega(\Delta x)^2} \right) + \Delta t^n \alpha_{i,3} \right] C_{i,3}(\{p_{\boldsymbol{j}}^n\}_{\boldsymbol{j}}) + \left[\frac{1}{2|\mathcal{I}|} \left(1 - \Delta t^n h_{\boldsymbol{j}}^n - \sum_{i\in\mathcal{I}} \frac{\Delta t^n (r_i)_{\boldsymbol{j}}^n}{\Omega(\Delta x)^2} \right) + \Delta t^n \alpha_{i,4} \right] C_{i,4}(\{p_{\boldsymbol{j}}^n\}_{\boldsymbol{j}}). \tag{61}$$

Guaranteeing that the coefficients of the $C_{i,k}$ terms are non-negative requires a sufficiently small Δt^n. In light of the bound (58), it suffices for Δt^n to satisfy, for example,

$$\Delta t^n \left[\|h\|_\infty + \frac{R_\infty}{\Delta x} \left(\frac{1}{\Omega \Delta x} + 4|\mathcal{I}| \right) \right] \le 1, \qquad \text{for} \qquad R_\infty = \sum_{i\in\mathcal{I}} \|r_i\|_\infty. \tag{62}$$

Condition (62) guarantees that, for each discrete state, the scheme is monotonic with respect to the homogeneous terms. The terms in the square brackets in (62) have direct interpretations: the first term represents the zeroth order exponential contributions of h from (56) and the second term represents the contributions from the higher order differential terms. This latter term comprises two contributions in the round brackets, the first comes from the second-order term and the second from the first-order terms.

B Code example

In this appendix, we illustrate the Python implementation of the reaction networks (6) and (7), which comprise reactions, non-local bursting, and discrete states. Each network is reproduced alongside the code required to simulate the evolution of the distribution in Fig. 8.

The implementation of each network in the Flips software is a straightforward encoding of the network diagram: mRNA molecules are represented by the label `'m'`, protein molecules by the label `'p'`. A `solver`

Reaction network (6):

$$\begin{aligned} \varnothing &\xrightarrow{\text{Hill(Protein)}} \text{mRNA}, \\ \text{mRNA} &\xrightarrow{\gamma B} \text{mRNA} + \text{Protein}, \\ \text{mRNA} &\xrightarrow{\gamma} \varnothing, \\ \text{Protein} &\xrightarrow{\gamma_0} \varnothing. \end{aligned}$$

Python code:

```
crn = solver([
    [{'m':1}, {'m':1,'p':1}, gamma*B],
    [{'p':1}, {}, gamma0],
], discrete_truncs={'m':2}, discrete_reactions=[
    [{}, {'m':1}, Hill('p', n=n, shift=r0, coeff=r1)],
    [{'m':1}, {}, gamma],
], diffusion=0)

crn.set_initial_conditions('uniform')
crn.solve(30)
crn.plot_p()
```

(a)

Reaction network (7):

$$\begin{aligned} \varnothing &\xrightarrow{\text{burst(Hill(Protein),}B)} \text{Protein}, \\ \text{Protein} &\xrightarrow{\gamma_0} \varnothing. \end{aligned}$$

Python code:

```
crn = flips.solver([
    [{}, {'p':1}, burst(Hill('p', n=n, shift=r0, coeff=r1), B)],
    [{'p':1}, {}, gamma0],
], diffusion=0)

crn.set_initial_conditions('uniform')
crn.solve(30)
crn.plot_p()
```

(b)

Figure 8: Python code to simulate the reaction networks from Section 3.1.

object is created with the network structure, reactions are separated into those governing continuum species and those governing discrete states (for which a finite truncation is specified). Each reaction includes three pieces of information: the reactants, the products, and the reaction rate. Additionally, since we follows models in the limit as $\Omega \to \infty$, the diffusion is eliminated by setting `diffusion=0`. Finally, an initial distribution is set, the distribution is evolved until some time, and the result plotted.

The interface is a direct translation of the network diagram, and therefore accessible to the non-technical user. Simultaneously, options for the advanced user allow fine tuning of the state and time discretisation (see [14]).

C Hermite equation

In this appendix, we seek separable solutions of equation (17), which we reproduce here:

$$\frac{\partial}{\partial t}q(x,t) = -\frac{\partial}{\partial x}[(\lambda(x)-\mu(x))q(x,t)] + \frac{1}{2\Omega}\frac{\partial^2}{\partial x^2}[(\lambda(x)+\mu(x))q(x,t)] + G(x)q(x,t). \tag{63}$$

Writing $q = T(t)X(x)$, and substituting into (63) it follows that

$$\frac{1}{T(t)}\frac{\mathrm{d}}{\mathrm{d}t}T(t) = -\frac{1}{X(x)}\frac{\mathrm{d}}{\mathrm{d}x}[(\lambda(x)-\mu(x))X(x)] + \frac{1}{2\Omega}\frac{1}{X(x)}\frac{\mathrm{d}^2}{\mathrm{d}x^2}[(\lambda(x)+\mu(x))X(x)] + G(x). \tag{64}$$

The left-hand side is a function only of t, while the right-hand side is a function only of x, therefore these must both be constant, taking the value of the growth rate, which we will denote r. This is sometimes called the Malthus parameter [11]. In other words, $T(t) = T(0)\mathrm{e}^{rt}$, and

$$-\frac{\mathrm{d}}{\mathrm{d}x}[(\lambda(x)-\mu(x))X(x)] + \frac{1}{2\Omega}\frac{\mathrm{d}^2}{\mathrm{d}x^2}[(\lambda(x)+\mu(x))X(x)] + (G(x)-r)X(x) = 0. \tag{65}$$

Equation (65) is of Sturm–Liouville form, and does not have, in general, a closed-form solution. We are not aware of a closed-form solution for birth and death functions (20) even in the linear-growth case of $G(x) = gx$. Nonetheless, we may seek an asymptotic approximation in the limit as $\Omega \to \infty$. As

explored in [38], the leading-order outer solution concentrates the probability mass at the critical point x_c. There was no growth term in [38], however, while this influences the growth along the characteristics, the characteristics themselves are not affected and thus the same singular evolution unfolds in our case. This singular perturbation is regularised within a boundary layer in the vicinity of the critical point, by considering the scaling

$$x = x_c + \xi \frac{1}{\sqrt{\Omega}} \sqrt{\frac{\lambda(x_c) + \mu(x_c)}{-(\lambda'(x_c) - \mu'(x_c))}}. \tag{66}$$

The leading-order inner form of (65) is then given by

$$X''(\xi) + 2\xi X'(\xi) + 2(\ell + 1)X(\xi) = 0, \tag{67}$$

where we assume that x_c is a simple root of $\lambda - \mu$, primes denoting differentiation with respect to the argument, and the constant ℓ is given by

$$\ell = \frac{g(x_c) - r}{-(\lambda'(x_c) - \mu'(x_c))}. \tag{68}$$

Equation (67) may be transformed to the Hermite equation under the transformation

$$Y(\xi) = \mathrm{e}^{\xi^2} X(\xi), \tag{69}$$

whereby

$$Y''(\xi) - 2\xi Y'(\xi) + 2\ell Y(\xi) = 0. \tag{70}$$

We now demonstrate that admissable solutions of the Hermite equation (70) may be found if ℓ is a non-negative integer. We seek a formal series solution of the form

$$Y(\xi) = \sum_{i=0}^{\infty} c_i \xi^i. \tag{71}$$

Upon substituting (71) into (70) and matching coefficients of the powers of ξ, we obtain the recurrence relation

$$c_{i+2} = \frac{2(i - \ell)}{(i + 1)(i + 2)} c_i. \tag{72}$$

The recurrence relation (72) expresses a dependence of coefficients on those indexed of the same parity. Therefore, each coefficient c_i may be expressed as a function of either c_0 or c_1, for i even or odd, respectively. The values for c_0 and c_1 may be determined by conditions at, say, the origin:

$$Y(0) = c_0, \qquad\qquad Y'(0) = c_1. \tag{73}$$

We argue, on physical grounds, that we expect the leading-order inner solution to be symmetric about the origin, whereby $Y'(0) = 0 = c_1$, and thus all odd coefficients vanish. For a non-negative integer $\ell \geq 0$, we see from (72) that $c_\ell = 0$, from which it follows that $c_{\ell+2j} = 0$ for all $j \geq 0$. Thus the series terminates at ℓth order to give a polynomial. These polynomials are called Hermite polynomials. Further properties of the Hermite polynomials and connections to other special functions are discussed in [45]. For many applications, this family of polynomial solutions is the only admissible solution, as other values of ℓ lead to solutions that are not polynomially bounded. However, in our case the justification must be slightly stronger, since from (69) we see that Y can grow in the far field and X may still vanish. Since the outer solution concentrates probability mass in the vicinity of the stable equilibrium, we expect it to be zero to all orders at asymptotically large time. On this basis, we now demonstrate that solutions for values of ℓ other than the non-negative integers are inadmissible.

Consider the series solution in Y for $0 < \ell \notin \mathbb{Z}$, and denote the smallest odd integer larger than ℓ by $2L - 1$. Since only even indices c_i are nonzero, it follows that

$$Y(\xi) = \sum_{i=0}^{\infty} c_{2i} \xi^{2i} = \sum_{i=0}^{\infty} \frac{d_i (\xi^2)^i}{i!}, \qquad \text{for} \qquad d_i = c_{2i} i!. \tag{74}$$

We bound d_i by noting from (72) that, for $i > L$,

$$\begin{aligned}
|d_i| &= \left|\frac{2^i(2i-2-\ell)(2i-4-\ell)\cdots(2-\ell)(-\ell)c_0 i!}{(2i)!}\right| \\
&> \left|\frac{2^i(2i-2-(2L-1))(2i-4-(2L-1))\cdots(2-(2L-1))(-(2L-1))c_0 i!}{(2i)!}\right| \\
&= \frac{2^i i!(2i-1-2L)(2i-3-2L)\cdots(3)(1)}{(2i)!}\left|(-1)(-3)\cdots(-(2L-1))c_0\right| \\
&= \frac{1}{(2i-1)(2i-3)\cdots(2i+1-2L)}\left|(-1)^L(2L-1)!!c_0\right| \\
&= \frac{1}{(i+1)(i+2)\cdots(i+L)}\frac{(i+1)(i+2)\cdots(i+L)}{(2i-1)(2i-3)\cdots(2i+1-2L)}(2L-1)!!|c_0| \\
&> \frac{1}{(i+1)(i+2)\cdots(i+L)}C_L,
\end{aligned} \tag{75}$$

where $C_L = (2L-1)!!|c_0|/2^L$ and is independent of i. We thus deduce that

$$\begin{aligned}
|Y(\xi)| + \sum_{i=0}^{L}\frac{|d_i|(\xi^2)^i}{i!} \geq \left|Y(\xi) - \sum_{i=0}^{L}\frac{d_i(\xi^2)^i}{i!}\right| &> \sum_{i=L+1}^{\infty}\frac{C_L(\xi^2)^i}{(i+L)!} \\
&= \sum_{i=0}^{L}\left(-\frac{C_L}{(i+L)!}\right)(\xi^2)^i + \frac{C_L}{\xi^{2L}}\sum_{i=0}^{\infty}\frac{(\xi^2)^{i+L}}{(i+L)!} \\
&= \sum_{i=-L}^{L} D_i(\xi^2)^i + \frac{C_L}{\xi^{2L}}\,\mathrm{e}^{\xi^2},
\end{aligned} \tag{76}$$

for constants D_i. Substituting the bound (76) into (69), we find that

$$|X(\xi)| > \mathrm{e}^{-\xi^2}\sum_{i=-L}^{L}\hat{D}_i(\xi^2)^i + \frac{C_L}{\xi^{2L}}, \tag{77}$$

for other constants $\hat{D}_i$. The second term on the right-hand side of (77) is not beyond all orders for any L, therefore, such a solution X cannot match the outer solution and we neglect it. For $\ell < 0$, Y diverges more rapidly in the far field, since $Y(\xi;\ell)$ is monotonically increasing with respect to $\ell \notin \{0 \leq n \in \mathbb{Z}\}$. In fact, for $\ell = -1$ it turns out that $Y(\xi) = \mathrm{e}^{\xi^2}$, and X is constant. In summary, only solutions for non-negative integer ℓ are admissible.

The growth rates r_ℓ corresponding to mode ℓ are given by

$$r_\ell = g(x_c) + \ell(\lambda'(x_c) - \mu'(x_c)). \tag{78}$$

The sequence r_ℓ is monotonically decreasing (since at a stable equilibrium $\lambda' - \mu' < 0$), therefore, for large times, the $\ell = 0$ mode will be dominant, dictating both the functional form and the growth rate. We thus deduce that the large-time behaviour will be described by constant $Y(\xi)$, and thus

$$X(x) = C\mathrm{e}^{-(x-x_c)^2/(a\Omega)}, \tag{79}$$

where C is a normalisation constant, given by $C = 1/\sqrt{a\Omega\pi}$ for X to be a probability density. The profile is a Gaussian centred at $x = x_c$ of width $\mathcal{O}(1/\sqrt{a\Omega})$. The growth rate is approximated by r_0, namely

$$r_0 = G(x_c) = g(1 - 1/\Lambda). \tag{80}$$

The last equality is for the specific forms $G(x) = gx$ and the functions in (20). Defining the shorthand

$$P_0 = \int_0^\infty q(x,t)\,\mathrm{d}x, \tag{81}$$

and integrating (18), we find that

$$\frac{P_0'(t)}{P_0(t)} = \frac{\int_0^\infty G(x)q(x,t)\,\mathrm{d}x}{\int_0^\infty q(x,t)\,\mathrm{d}x}, \tag{82}$$

that is, the growth rate is given by the G-moment of the q density. For the separable solution $q = TX = \mathrm{e}^{r_0 t}X(x)$, we see that

$$\frac{P_0'(t)}{P_0(t)} = \frac{1}{T}\frac{\mathrm{d}T}{\mathrm{d}t} = r_0, \tag{83}$$

from which it follows that the G-moment of p_0 is precisely r_0.

D Fragmentation models

In this appendix, we discuss analytical and numerical aspects of the growth–fragmentation equation (24), which we rewrite here:

$$\frac{\partial}{\partial t}\rho(x,t) = -\frac{\partial}{\partial x}[g(x,t)\rho(x,t)] - B(x,t)\rho(x,t) + \int_x^\infty b(y,x,t)\rho(y,t)\,\mathrm{d}y. \tag{84}$$

First, we demonstrate that ensuring the fragmentation splits one cell into two while conserving volume is achieved by imposing the constraints [11]

$$2B(x,t) = \int_0^x b(x,z,t)\,\mathrm{d}z, \qquad\qquad xB(x,t) = \int_0^x zb(x,z,t)\,\mathrm{d}z, \tag{85}$$

respectively. Consistency further requires that the rate (per unit size) of cell division for cells of size y into cells of size x and $y-x$ is equal, that is,

$$b(y,x,t) = b(y,y-x,t). \tag{86}$$

From (84), we find that the rate of change of the number of cells in the system is governed by

$$\frac{\mathrm{d}}{\mathrm{d}t}\int_0^\infty \rho(x,t)\,\mathrm{d}x = -\int_0^\infty \frac{\partial}{\partial x}[g(x,t)\rho(x,t)]\,\mathrm{d}x - \int_0^\infty B(x,t)\rho(x,t)\,\mathrm{d}x + \int_0^\infty\int_x^\infty b(y,x,t)\rho(y,t)\,\mathrm{d}y\,\mathrm{d}x. \tag{87}$$

The first term on the right-hand side of (87) vanishes due to the no-flux and vanishing far-field conditions. In fact, it follows that we need $\rho(x,t) = o\left([xg(x,t)]^{-1}\right)$ as $x \to \infty$. By changing the order of integration and using the first condition (85), we find that

$$\frac{\mathrm{d}}{\mathrm{d}t}\int_0^\infty \rho(x,t)\,\mathrm{d}x = -\int_0^\infty B(x,t)\rho(x,t)\,\mathrm{d}x + \int_0^\infty \rho(y,t)\int_0^y b(y,x,t)\,\mathrm{d}x\,\mathrm{d}y = \int_0^\infty B(x,t)\rho(x,t)\,\mathrm{d}x. \tag{88}$$

The rate of change of volume in the system is governed by

$$\begin{aligned}\frac{\mathrm{d}}{\mathrm{d}t}\int_0^\infty x\rho(x,t)\,\mathrm{d}x = &-\int_0^\infty x\frac{\partial}{\partial x}[g(x,t)\rho(x,t)]\,\mathrm{d}x \\ &-\int_0^\infty xB(x,t)\rho(x,t)\,\mathrm{d}x + \int_0^\infty\int_x^\infty xb(y,x,t)\rho(y,t)\,\mathrm{d}y\,\mathrm{d}x.\end{aligned} \tag{89}$$

By changing the order of integration in the final term on the right-hand side of (89) and using the second condition (85), we find that the second and third terms cancel, thus

$$\frac{\mathrm{d}}{\mathrm{d}t}\int_0^\infty x\rho(x,t)\,\mathrm{d}x = -\int_0^\infty x\frac{\partial}{\partial x}[g(x,t)\rho(x,t)]\,\mathrm{d}x = \int_0^\infty g(x,t)\rho(x,t)\,\mathrm{d}x, \tag{90}$$

where we again used the no-flux and vanishing far-field conditions.

The calculations confirm the physical features of the model: the rate of change of the number of cells (88) is given by the average rate of fragmentation B, but independent of the growth g, while the rate of change of volume (90) is given by the average growth rate g, but independent of fragmentation.

Given a kernel b, we may derive B via one of the conditions in (85), however, the other condition in (85) as well as condition (86) still constrain b in a highly non-trivial way. With the aim of simplifying the fragmentation description, as well as bringing it in line with the framework based on system (5), we introduce a new representation of the fragmentation function b (from which we will derive B) that will decouple the constraints without loss of generality. We define

$$b(y, x, t) = 2r(y, t)f_y(x, t), \tag{91}$$

where r is the fragmentation rate of cells of size y, and f_y is the probability density that the fragmentation of a cell of size y produces a cell of size x. We define the corresponding cumulative probability function F_y via

$$F_y(x, t) = \int_0^x f_y(z, t)\,\mathrm{d}z, \tag{92}$$

and note that

$$F_y(y, t) = 1. \tag{93}$$

We satisfy the symmetry condition (86) by requiring that

$$f_y(x, t) = f_y(y - x, t). \tag{94}$$

We may satisfy conditions (85) by requiring that

$$2B(x, t) = \int_0^x 2r(x, t)f_x(z, t)\,\mathrm{d}z = 2r(x, t), \tag{95}$$

and

$$xB(x, t) = \int_0^x 2zr(x, t)f_x(z, t)\,\mathrm{d}z = 2r(x, t)\int_0^x zf_x(z, t)\,\mathrm{d}z = 2r(x, t)\left[x - \int_0^x F_x(z, t)\,\mathrm{d}z\right], \tag{96}$$

where the last equality comes from integrating by parts and using (93). From (95) we see why r was introduced as twice the fragmentation rate. Upon substituting (95) into (96), the constraint takes the form

$$\int_0^x F_x(z, t)\,\mathrm{d}z = \frac{x}{2}. \tag{97}$$

We proceed to show how constraint (97) is satisfied by the representation (91). From the probability property (93) and the symmetry condition (94) we see that

$$F_x(z, t) = \int_0^z f_x(s)\,\mathrm{d}s = \int_0^z f_x(x - s)\,\mathrm{d}s = \int_{x-z}^x f_x(s)\,\mathrm{d}s = F_x(x, t) - F_x(x - z, t) = 1 - F_x(x - z, t), \tag{98}$$

from which it follows that

$$\begin{aligned}
\int_0^x F_x(z, t)\,\mathrm{d}z &= \int_0^{x/2} F_x(z, t)\,\mathrm{d}z + \int_{x/2}^x F_x(z, t)\,\mathrm{d}z \\
&= \int_0^{x/2} F_x(z, t)\,\mathrm{d}z + \int_{x/2}^x 1 - F_x(x - z, t)\,\mathrm{d}z \\
&= \int_0^{x/2} F_x(z, t)\,\mathrm{d}z + \frac{x}{2} - \int_0^{x/2} F_x(z, t)\,\mathrm{d}z \\
&= \frac{x}{2}.
\end{aligned} \tag{99}$$

To recap, by introducing the representation (91) for b based on a decomposition into a rate and a symmetric probability density, we trivially satisfy both conditions in (85) and condition (86). The fragmentation rate B is equivalent to the rate r in this representation. Importantly, this representation expresses the kernel b in terms of identifiable quantities. In particular, the practitioner needs to specify

the rate r at which fragmentation occurs for each cell size, and the distribution of fragments f_y. There are additional advantages to this representation. This formulation allows for a straightforward description of self-similar fragmentation kernels, that is, the dependence of f_y on y is only a rescaling, namely

$$f_y(x,t) = \frac{1}{y} f(x/y, t), \tag{100}$$

where $f(x,t)$ is a density on $z \in (0,1)$. For example, symmetric or asymmetric mitosis is commonly modeled with cell division resulting in cells whose size is distributed proportionally to the original cell [11]. Moreover, it is easy to incorporate Dirac delta functions within f_y since the finite-volume scheme is built via integrating over finite regions of the state space. Therefore, the cumulative representation of f_y via F_y suffices, and this is a well-defined function. To see this, we detail the discretisation of the fragmentation operator.

As with bursts, for each volume centred at $i\Delta x$ we subtract the propensity of fragmenting to within the volume centred at $j\Delta x$ for $0 \leq j < i$ and add that propensity to the j volume, thereby achieving conservation of volume. Note that in this paragraph we have used the word "volume" to refer to what is normally called a "cell", so as not to confuse the use of the word "cell" elsewhere in this paper referring to the biological entity. The probability of fragmenting from j to i is given by

$$\begin{aligned}\mathbb{P}(\text{fragment } j \to i) &= \int_{(j-1/2)\Delta x}^{(j+1/2)\Delta x} \int_{(i-1/2)\Delta x}^{(i+1/2)\Delta x} f_y(x,t)\,\mathrm{d}x\,\mathrm{d}y \\ &= \int_{(j-1/2)\Delta x}^{(j+1/2)\Delta x} F_y((i+1/2)\Delta x, t) - F_y((i-1/2)\Delta x, t)\,\mathrm{d}y. \end{aligned} \tag{101}$$

The probability (101) is expressed via its cumulative density. Further simplification is possible, for example, in the self-similar case,

$$\mathbb{P}(\text{fragment } j \to i) = \frac{1}{\Delta x} \int_0^1 F\left(\frac{i+1/2}{j-1/2+Y}, t\right) - F\left(\frac{i-1/2}{j-1/2+Y}, t\right) \mathrm{d}Y. \tag{102}$$

If the distribution is only Dirac masses, for example, time-invariant asymmetric mitosis at size fractions c and $1-c$ for $c \in (0,1)$, then $f(x,t) = [\delta(x-c) + \delta(x-1+c)]/2$, in which case (102) further simplifies to

$$\begin{aligned}\mathbb{P}(\text{fragment } j \to i) &= \frac{1}{2\Delta x} \int_0^1 \mathbb{1}_{(i+1/2)/c-(j-1/2)>Y} + \mathbb{1}_{(i+1/2)/(1-c)-(j-1/2)>Y} \\ &\qquad - \mathbb{1}_{(i-1/2)/c-(j-1/2)>Y} - \mathbb{1}_{(i-1/2)/(1-c)-(j-1/2)>Y}\,\mathrm{d}Y \\ &= \frac{1}{2\Delta x}\Big[Q((i+1/2)/c-(j-1/2)) + Q((i+1/2)/(1-c)-(j-1/2)) \\ &\qquad - Q((i-1/2)/c-(j-1/2)) - Q((i-1/2)/(1-c)-(j-1/2))\Big], \end{aligned} \tag{103}$$

where $\mathbb{1}_{x>0}$ is the Heaviside function and Q is the integral

$$Q(c) = \int_0^1 \mathbb{1}_{x<c}\,\mathrm{d}x = \min(1, \max(0, c)). \tag{104}$$

The formula (103) accelerates construction of the scheme since no integrals need to be computed, and demonstrates how Dirac delta functions are accurately captured in the finite volume discretisation. The fragmentation probability is multiplied by the fragmentation rate r to give the local fragmentation propensity, and probability mass is transferred from volume j in proportion to the propensity, to volume i with twice this proportion to account for the cell creation (this is the factor of 2 in (91)).

E An explicit growth–fragmentation solution

In this appendix, we compile analytical solutions of growth–fragmentation equations for benchmark use. We begin by considering the growth-free problem considered in [39], namely

$$\frac{\partial}{\partial t}\rho(x,t) = \int_x^\infty 2ay^{k-1}\rho(y,t)\,\mathrm{d}y - ax^k\rho(x,t). \tag{105}$$

The equation (105) corresponds to the growth–fragmentation model (24) with no growth $g \equiv 0$ and fragmentation kernel $b(y,x) = 2ay^{k-1}$, from which we deduce, via (85), that $B(x) = ax^k$.

We refer the reader to [39] for a step-by-step solution of (105). In brief, we seek a similarity solution of the form

$$\rho(x,t) = x^\alpha h(\eta), \qquad \eta = xt^\beta. \tag{106}$$

It can be shown that the scalings must satisfy $\alpha = -2$ and $\beta = 1/k$. The equation (105) may then be reduced to an ODE for h, admitting the solution

$$\rho(x,t) = x^{-2}h(\eta) = c(at)^{2/k}\mathrm{e}^{-atx^k}, \tag{107}$$

where c is an arbitrary constant.

We now employ a change of variables presented in [40] which transforms the solution of the general growth-free equation

$$\frac{\partial}{\partial t}\rho(x,t) = \int_x^\infty b(y,x)\rho(y,t)\,\mathrm{d}y - B(x)\rho(x,t), \tag{108}$$

such as (105), to the solution of a growth–fragmentation equation with non-uniform growth and uniform degradation. We assume that the fragmentation kernel is time-invariant homogeneous of degree $\gamma - 1$ for $\gamma > 0$, that is,

$$b(sy, sx) = s^{\gamma-1}b(x,y), \tag{109}$$

for any $s > 0$. For equation (105) the kernel is homogeneous with $\gamma = k$.

We now define

$$\hat\rho(x,t) = \mathrm{e}^{-2t}\rho(\mathrm{e}^{-t}x, \mathrm{e}^{\gamma t} - 1), \tag{110}$$

and look for an equation governing the time evolution of $\hat\rho$ by taking partial derivatives. First with respect to x, we find that

$$\frac{\partial}{\partial x}\hat\rho(x,t) = \mathrm{e}^{-3t}\frac{\partial\rho}{\partial x}(\mathrm{e}^{-t}x, \mathrm{e}^{kt} - 1). \tag{111}$$

Then, using the dynamics (105), and (111), we see that

$$\begin{aligned}\frac{\partial}{\partial t}\hat\rho(x,t) &= -2\mathrm{e}^{-2t}\rho(\mathrm{e}^{-t}x, \mathrm{e}^{kt} - 1) - \mathrm{e}^{-3t}x\frac{\partial\rho}{\partial x}(\mathrm{e}^{-t}x, \mathrm{e}^{kt} - 1) + k\mathrm{e}^{(k-2)t}\frac{\partial\rho}{\partial t}(\mathrm{e}^{-t}x, \mathrm{e}^{kt} - 1)\\ &= -2\hat\rho(x,t) - x\frac{\partial}{\partial x}\hat\rho(x,t) + k\mathrm{e}^{(k-2)t}\times\\ &\qquad\left[\int_{\mathrm{e}^{-t}x}^\infty b(y, \mathrm{e}^{-t}x, \mathrm{e}^{kt} - 1)\rho(y, \mathrm{e}^{kt} - 1)\,\mathrm{d}y - B(\mathrm{e}^{-t}x)\rho(\mathrm{e}^{-t}x, \mathrm{e}^{kt} - 1)\right].\end{aligned} \tag{112}$$

Upon substituting (110), changing variables, and using homogeneity assumption (108), the square brackets on the right-hand side of (112) may be expressed as

$$\begin{aligned}&\int_{\mathrm{e}^{-t}x}^\infty b(y, \mathrm{e}^{-t}x)\rho(y, \mathrm{e}^{kt} - 1)\,\mathrm{d}y - B(\mathrm{e}^{-t}x)\rho(\mathrm{e}^{-t}x, \mathrm{e}^{kt} - 1)\\ &\qquad= \mathrm{e}^t\int_x^\infty b(\mathrm{e}^{-t}z, \mathrm{e}^{-t}x)\hat\rho(z,t)\,\mathrm{d}z - \mathrm{e}^{(2-k)t}B(x)\hat\rho(x,t)\\ &\qquad= \mathrm{e}^{(2-k)t}\left[\int_x^\infty b(z,x)\hat\rho(z,t)\,\mathrm{d}z - B(x)\hat\rho(x,t)\right],\end{aligned} \tag{113}$$

whereby we see that $\hat\rho$ satisfies the growth–fragmentation equation

$$\frac{\partial}{\partial t}\hat\rho(x,t) = -\frac{\partial}{\partial x}\left[x\hat\rho(x,t)\right] - \hat\rho(x,t) + k\left[\int_x^\infty b(z,x)\hat\rho(z,t)\,\mathrm{d}z - B(x)\hat\rho(x,t)\right]. \tag{114}$$

Equation (114) captures growth linear in the cell size x and uniform decay. Using b (and thus B) from equation (105) means that $\hat\rho$ describes a process that inherits an analogous fragmentation behaviour occuring at k times the rate.

Acknowledgements

This work was partially supported by the Inria Project Lab CoSy and by the ANR grants ANR-18-CE91-0002 (CyberCircuits) and ANR-16-CE33-0018 (MEMIP).

References

[1] D. T. Gillespie. A rigorous derivation of the chemical master equation. *Physica A*, 188(1):404–425, 1992.

[2] D. T. Gillespie. The chemical Langevin equation. *J. Chem. Phys.*, 113(1):297–306, 2000.

[3] W. Weidlich and G. Haag. *Concepts and models of a quantitative sociology: the dynamics of interacting populations*, volume 14. Springer Science & Business Media, 2012.

[4] D. Fraser and M. Kærn. A chance at survival: gene expression noise and phenotypic diversification strategies. *Mol. Microbiol.*, 71(6):1333–1340, 2009.

[5] A. Eldar and M. B. Elowitz. Functional roles for noise in genetic circuits. *Nature*, 467(7312):167–173, 2010.

[6] P. D. Tonner, C. L. Darnell, F. M. L. Bushell, P. A. Lund, A. K. Schmid, and S. C. Schmidler. A Bayesian non-parametric mixed-effects model of microbial growth curves. *PLOS Comput. Biol.*, 16(10):1–21, 10 2020.

[7] C.-C. Shu, A. Chatterjee, G. Dunny, W.-S. Hu, and D. Ramkrishna. Bistability versus bimodal distributions in gene regulatory processes from population balance. *PLOS Comput. Biol.*, 7(8):1–13, 08 2011.

[8] T. Mora and A. M. Walczak. Effect of phenotypic selection on stochastic gene expression. *J. Phys. Chem. B*, 117(42):13194–13205, 2013. PMID: 23795617.

[9] K. Sato and K. Kaneko. On the distribution of state values of reproducing cells. *Phys. Biol.*, 3(1):74–82, mar 2006.

[10] L. Duso and C. Zechner. Stochastic reaction networks in dynamic compartment populations. *Proc. Natl. Acad. Sci. U.S.A.*, 2020.

[11] B. Perthame. *Transport equations in biology*. Birkhäuser Basel, 2006.

[12] N. Friedman, L. Cai, and X. S. Xie. Linking stochastic dynamics to population distribution: An analytical framework of gene expression. *Phys. Rev. Lett.*, 97:168302, Oct 2006.

[13] J.-B. Bardet, A. Christen, A. Guillin, F. Malrieu, and P.-A. Zitt. Total variation estimates for the TCP process. *Electron. J. Probab.*, 18, 2013.

[14] D. Lunz. Flips solver repository. https://gitlab.inria.fr/dlunz/flips, 2020.

[15] C. Gardiner. *Stochastic Methods: A Handbook for the Natural and Social Sciences*. Springer Series in Synergetics. Springer Berlin Heidelberg, third edition, 2009.

[16] H. Risken. *Fokker–Planck Equation*. Springer Berlin Heidelberg, Berlin, Heidelberg, 1996.

[17] D. J. Aldous. Deterministic and stochastic models for coalescence (aggregation, coagulation): a review of the mean-field theory for probabilists. *Bernoulli*, 5:3–48, 1997.

[18] F. Kawano, R. Okazaki, M. Yazawa, and M. Sato. A photoactivatable Cre–loxP recombination system for optogenetic genome engineering. *Nat. Chem. Biol.*, 12(12):1059–1064, 2016.

[19] D. T. Gillespie. A general method for numerically simulating the stochastic time evolution of coupled chemical reactions. *J. Comput. Phys.*, 22(4):403–434, 1976.

[20] D. T. Gillespie. Exact stochastic simulation of coupled chemical reactions. *J. Phys. Chem.*, 81(25):2340–2361, 1977.

[21] M. A. Gibson and J. Bruck. Efficient exact stochastic simulation of chemical systems with many species and many channels. *J. Phys. Chem. A*, 104(9):1876–1889, 2000.

[22] D. T. Gillespie. Approximate accelerated stochastic simulation of chemically reacting systems. *J. Chem. Phys.*, 115(4):1716–1733, 2001.

[23] A. Hellander and P. Lötstedt. Hybrid method for the chemical master equation. *J. Comput. Phys.*, 227(1):100–122, 2007.

[24] Y. Cao, D. T. Gillespie, and L. R. Petzold. The slow-scale stochastic simulation algorithm. *J. Chem. Phys.*, 122(1):014116, 2005.

[25] B. Munsky and M. Khammash. The finite state projection algorithm for the solution of the chemical master equation. *J. Chem. Phys.*, 124(4):044104, 2006.

[26] S. Peleš, B. Munsky, and M. Khammash. Reduction and solution of the chemical master equation using time scale separation and finite state projection. *J. Chem. Phys.*, 125(20):204104, 2006.

[27] S. W. Wang, P. G. Georgopoulos, G. Li, and H. Rabitz. Condensing complex atmospheric chemistry mechanisms. 1. the direct constrained approximate lumping (DCAL) method applied to alkane photochemistry. *Environ. Sci. Technol.*, 32(13):2018–2024, 1998.

[28] S. Engblom. Spectral approximation of solutions to the chemical master equation. *J. Comput. Appl. Math.*, 229(1):208–221, 2009.

[29] T. Jahnke and T. Udrescu. Solving chemical master equations by adaptive wavelet compression. *J. Comput. Phys.*, 229(16):5724–5741, 2010.

[30] B. Hepp, A. Gupta, and M. Khammash. Adaptive hybrid simulations for multiscale stochastic reaction networks. *J. Chem. Phys.*, 142(3):034118, 2015.

[31] P. Sjöberg, P. Lötstedt, and J. Elf. Fokker–planck approximation of the master equation in molecular biology. *Comput. Vis. Sci.*, 12(1):37–50, 2009.

[32] L. Ferm, P. Lötstedt, and P. Sjöberg. Conservative solution of the fokker–planck equation for stochastic chemical reactions. *BIT*, 46(1):61–83, 2006.

[33] H. Salis and Y. Kaznessis. Accurate hybrid stochastic simulation of a system of coupled chemical or biochemical reactions. *J. Chem. Phys.*, 122(5):054103, 2005.

[34] E. L. Haseltine and J. B. Rawlings. Approximate simulation of coupled fast and slow reactions for stochastic chemical kinetics. *J. Chem. Phys.*, 117(15):6959–6969, 2002.

[35] C. Safta, K. Sargsyan, B. Debusschere, and H. N. Najm. Hybrid discrete/continuum algorithms for stochastic reaction networks. *J. Comput. Phys.*, 281:177–198, 2015.

[36] P. Sjöberg. PDE and Monte Carlo approaches to solving the master equation applied to gene regulation. Technical Report 2007-028, Uppsala University, Oct. 2007.

[37] Y. T. Lin and C. R. Doering. Gene expression dynamics with stochastic bursts: Construction and exact results for a coarse-grained model. *Phys. Rev. E*, 93:022409, Feb 2016.

[38] D. Lunz. On continuum approximations of continuous-time discrete-state markov processes of large system size. 2020. https://hal.inria.fr/hal-02560743.

[39] C. M. Rooney, I. M. Griffiths, C. Brunner, J. Potter, M. Wood-Lee, and C. P. Please. Dynamics of particle chopping in blenders and food processors. *J. Eng. Math.*, 112(1):119–135, 2018.

[40] M. J. Cáceres, J. A. Cañizo, and S. Mischler. Rate of convergence to an asymptotic profile for the self-similar fragmentation and growth-fragmentation equations. *J. Math. Pure Appl.*, 96(4):334–362, 2011.

[41] S. Brunner, T. Sauer, S. Carotta, M. Cotten, M. Saltik, and E. Wagner. Cell cycle dependence of gene transfer by lipoplex, polyplex and recombinant adenovirus. *Gene ther.*, 7(5):401–407, 2000.

[42] W.-C. Tseng, F. R. Haselton, and T. D. Giorgio. Mitosis enhances transgene expression of plasmid delivered by cationic liposomes. *BBA-Gene Struct. Expr.*, 1445(1):53–64, 1999.

[43] C. J. Zopf, K. Quinn, J. Zeidman, and N. Maheshri. Cell-cycle dependence of transcription dominates noise in gene expression. *PLOS Comput. Biol.*, 9(7):1–12, 07 2013.

[44] A. Kurganov and E. Tadmor. New high-resolution central schemes for nonlinear conservation laws and convection–diffusion equations. *J. Comput. Phys.*, 160(1):241–282, 2000.

[45] G. B. Arfken, H. J. Weber, and F. E. Harris. *Mathematical methods for physicists*. Academic Press, 7 edition, 2012.